UNIVERSITY OF COPENHAGEN
NIELS BOHR INSTITUTE

Master's thesis

Kristoffer Levin Hansen

Search for new physics in diphoton production with the ATLAS detector at the LHC

Academic advisor: Jørgen Beck Hansen

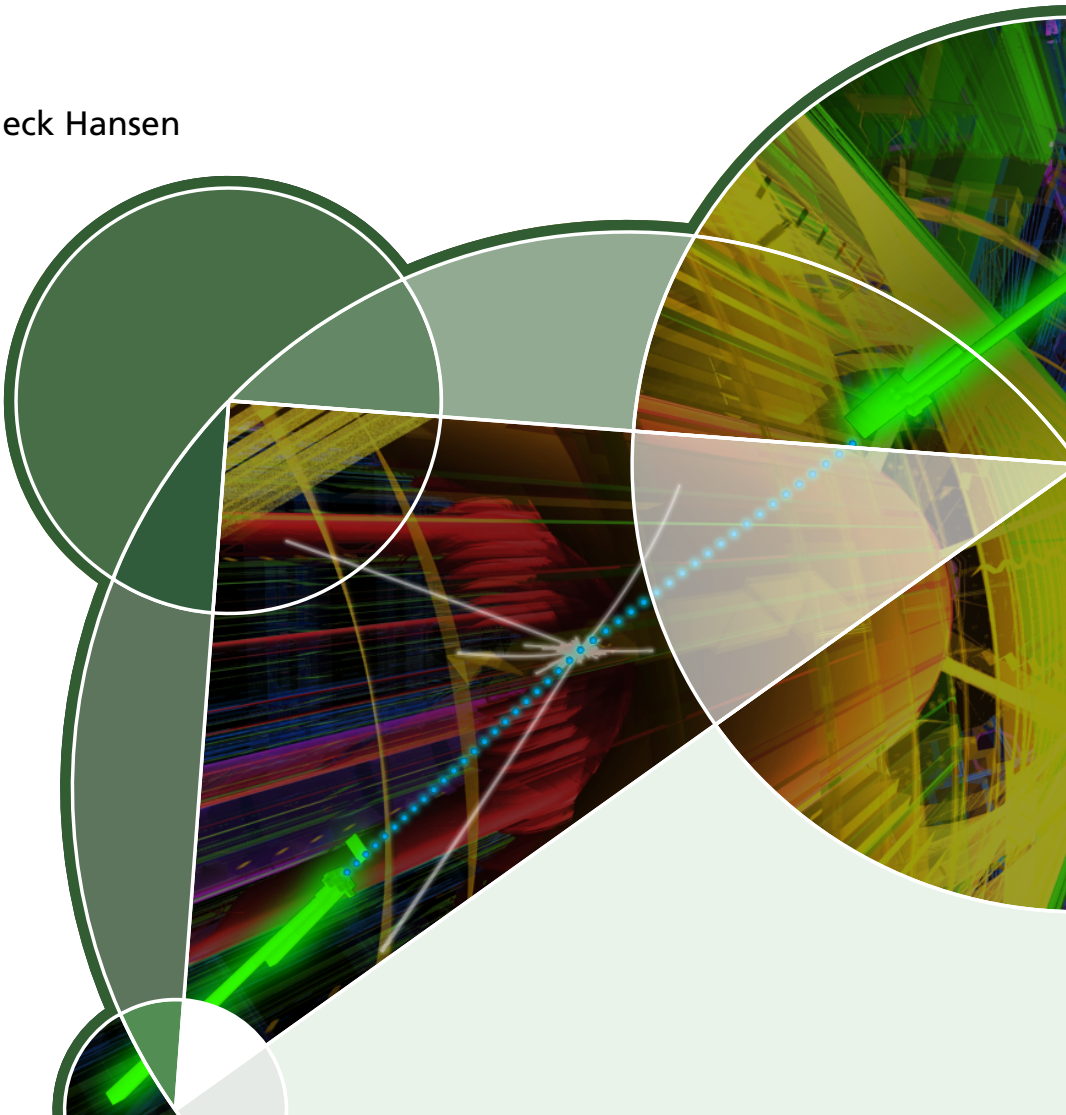

6th November 2015

“Art is never finished, merely abandoned.”

– Leonardo da Vinci

Abstract

In this thesis, we will conduct a search for physics beyond the Standard Model by introducing into it, via the effective Lagrangian approach, a new $qq\gamma\gamma$ contract interaction. The effects of this new interaction on the distribution of invariant masses of diphotons will be assessed via the production of Monte Carlo simulations at two values of the associated mass scale Λ, and a corresponding Monte Carlo set for the Standard Model. These Monte Carlo sets will be subjected to full ATLAS detector stimulation, before they are compared with data taken by ATLAS during the 2012, 8 TeV run of the LHC. A fully data driven background estimation will be carried out on this data set. Finally, we will interpolate our Monte Carlo samples, so that we may compare a distribution corresponding to any Λ with the experimental distribution. This can be used for a maximum profile likelihood fit of Λ to data.

Resumé på dansk

I dette speciale vil vi søge efter ny fysik ud over Standardmodellen, ved at indføre en ny $qq\gamma\gamma$ kontaktinteraktion ved brug af en effektiv Lagrangefunktion. Vi vil undersøge effekten af en sådan ny interaktion på fordelingen af invariante masser af difotoner produceret ved protonsammenstød, ved at fremstille Monte Carlo dataset ved to værdier af den tilhørende masseskala Λ, samt et korresponderende Monte Carlo sæt for Standardmodellen. Disse Monte Carlo sæt køres igennem den fulde ATLAS detektor simulering, før de sammenlignes med data taget af ATLAS under 8 TeV kørslen i LHC i 2012. En fuldt datadreven baggrundsestimering vil blive udført på det eksperimentelle data sæt. Endelig vil vi interpolere vores Monte Carlo datasæt, således at vi kan sammenligne distributioner der tilsvarer enhver værdi af Λ med den eksperimentelle distribution. På den måde kan et maksimal profil likelihood fit af Λ til data udføres.

Contents

1 Introduction

Since the late 1960s, our—at times evolving—understanding of the properties and interactions of the fundamental particles has been summarised by the Standard Model of Particle Physics. The Standard Model is formulated in the language of Quantum Field Theory[1], and attempts to combine a theoretical model of quantum mechanical phenomena with an experimental understanding of the properties of fundamental particles and the couplings between them.

An overview of a selection of these properties and interactions is given in fig. 1.1.

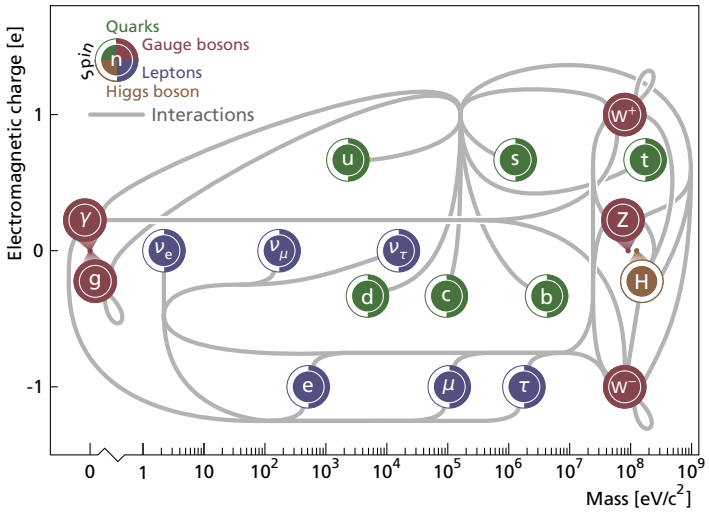

Figure 1.1: An overview of the particles of the Standard Model. The particles are arranged by mass and charge. Colour indicates particle type, the filling of the border indicates the spin of particles and lines are drawn between those particles that the Standard Model describes interactions between. The currently known maximum bounds on neutrino masses have been used to place the neutrinos in the mass direction. Table values from [1].

In its current form, the Standard Model makes no attempt to explain any physics beyond this.[2] The most obvious missing element is gravity, which finds no obvious expression in terms of Quantum Field Theory. Other seemingly missing elements come from astronomy, which bring observational evidence of a number of phenomena, such as dark matter and dark energy, which seem to require an explanation from within the

[1] Capitalised in anticipation of the imminent use of its common abbreviation, QFT.

[2] The overview in figure 1.1 includes massive neutrinos, which have been found experimentally, even though the Standard Model does not at present include them. There are, however, several proposed methods of extending the SM to do so.

realm of physics that the Standard Model describes, but for which the Standard Model offers no obvious source.

Disregarding these issues, which may be considered external its scope, the Standard Model has been remarkably successful as a model for high energy particle physics, withstanding decades of experimental tests and correctly predicting the existence and properties of several particles.[3] In spite of those successes, the Standard Model is not without its issues.

As it is formulated, the SM depends on at least 19 numerical constants,[4] the value of which must be determined experimentally, since the model offers no insight into the origin of or relations between them. Worse still, as the SM is a perturbative model, higher order corrections, which tend to increase the predicted Higgs mass with no constraint save the Planck energy, must be included in the theory. To arrive at the observed Higgs mass in spite of this tendency, either some unknown physics exist between the Higgs mass scale and the Planck scale to constrain the Higgs mass, or the bare mass and couplings of the Higgs boson are very finely tuned to cancel the higher order contributions. This is one example of the hierarchy problem.

In the first case, we will obviously want to search for evidence of the postulated new, high-energy physics. In the latter case, we might expect[5] there to be some additional mechanism within the Standard Model that ensures that the bare Higgs mass and the other free parameters of the SM are given the proper value. Again, we will want to search for physics outside what is currently described by the SM, as a clue to what that mechanism might be.

There is also the possibility that neither of those mechanisms exist, since the Standard Model, strictly speaking, does not require them. In that case a search for new physics that discovers nothing is still a valuable, albeit less illuminating, result.

In this thesis, we shall approach the task of searching for physics beyond the Standard Model by introducing to it an extension via the effective Lagrangian approach. Specifically, we will introduce a $q\bar{q} \to \gamma\gamma$ point interaction, and then simulate collision experiments with the new interaction at various strengths, to see how the outcome is affected. We can then, finally, compare the results of those pseudo-experiments to the results of actual collision experiments performed at CERN's Large Hadron Collider, and look for signs of the same effects there.

[3] Most recently, the existence of the Higgs boson was confirmed experimentally. At the time of writing, confirmation of its predicted properties is still a work in progress.

[4] Not counting any additional constants needed to account for neutrino masses.

[5] Or *hope for*, depending on how invested we happen to be in the question of fine–tuning.

2 Theory

While the detailed procedure for going from a general notion of expanding the Standard Model to creating a specific set of pseudoexperiments with which to compare experimental results are not part of the main thrust of this thesis, and will in any case be handled by various software tools in practice, what will follow is a brief overview of that process.

Since the new interaction will be introduced into the SM by the effective Lagrangian approach, the Lagrangian formulation of the Standard Model as a quantum field theory will be the starting point.

2.1 The Lagrangian formulation of QFT

In classical mechanics [2], the Lagrangian formulation describes the path taken by a system between a given initial and final state—a particle with an initial and a final position, say—by finding the path between these states that minimises the action S, which is defined as the integral along a given path over the Lagrangian L:

$$S[q] = \int_{\text{path}} dt L[q, \dot{q}],$$

where q is a generalised coordinate and a dot indicates a time derivative. In this picture, the Lagrangian encapsulates the dynamics of the system. It is related to the Hamiltonian H by

$$L = p\dot{q} - H, \tag{2.1}$$

where p is momentum.

In quantum mechanics, the picture of a system travelling along a single, well-defined path from an initial to a final configuration no longer applies. In stead, a probability of going from an initial state $|q\rangle$ to a final state $\left|q'\right\rangle$ can be found as the absolute square of the transition amplitude[1] [3]

$$A = \left\langle q' \right| e^{-i\hat{H}(t\prime - t)} \left| q \right\rangle,$$

where $\hat{H}$ is the Hamiltonian of the system. Since the idea of a singular path for the system was abandoned, in stead imagine the system travelling along each possible path

[1] At this point, we should note that the common notation where $\hbar = c = 1$ will be used from this chapter onwards.

simultaneously, each with its own transition amplitude. The total transition amplitude, then, is the sum of all the individual transition amplitudes. This can be connected to the classical case by supposing that, for a system with a classical limit, the transition amplitudes of paths close to the classical path will tend to amplify one another, while paths far from it will tend to cancel out.

Through some notational gymnastics, which involve carving the path integral into an infinite number of time steps, each integrated over every possible configuration, and imposing some conditions on the Lagrangian, it can be shown [3] that the expression above can be written as

$$A = \int \mathcal{D}q \, \exp\left[i \int_t^{t'} dt \, [p(t)\dot{q}(t) - H(p(t), q(t))] \right], \tag{2.2}$$

where the functional integral written $\int \mathcal{D}q$ is understood as the product of integrals over all paths with position q at time t and position q' at time t'. We recognise the expression in the innermost integral from eq. (2.1).

For a local theory, it is possible to write the Lagrangian as a spatial integral over the Lagrangian density:

$$L = \int d^3x \, \mathcal{L}.$$

Thus, the action can be written as

$$S = \int d^4x \, \mathcal{L}, \tag{2.3}$$

which, unlike the previous expression for S, is manifestly Lorenz invariant, so long as $\mathcal{L}$ is a Lorenz scalar. Given the ubiquity of local quantum field theories, it is common when discussing quantum field theory to drop 'density' from the name, and refer to $\mathcal{L}$ as the Lagrangian. Going forward, we will also follow that convention here.

Finally, to get the field theory aspect, replace the generalised coordinate q with a field configuration "coordinate" $\phi(x)$, which depends on the Lorenz vector x. In short, (2.2) can then be written as

$$A = \int \mathcal{D}\phi \, e^{iS[\phi]}. \tag{2.4}$$

As was the case in classical mechanics, the behaviour of a theory is fully described by its Lagrangian (density), and several models can be combined by adding together their respective Lagrangians. So it is that the Standard Model is described by the SM Lagrangian $\mathcal{L}_{SM}$, which can be considered as a sum of several lesser Lagrangians that describe the separate sectors of the SM.

2.2 The Standard Model Lagrangian

The Standard Model Lagrangian can be divided into sectors in several ways, according to the needs of the author [3, 1]. For this work, the sectors of the Standard Model shall be defined as follows,

$$\mathcal{L}_{SM} = \mathcal{L}_{EW} + \mathcal{L}_{QCD} + \mathcal{L}_{H}.$$

Thus, the SM has a sector which describes the electroweak part $\mathcal{L}_{EW}$, one which describes the QuantumChromoDynamics part $\mathcal{L}_{QCD}$ and one for the Higgs part $\mathcal{L}_{H}$.

The electroweak Lagrangian can be expanded to read as follows:

$$\mathcal{L}_{EW} = -\frac{1}{4} W^{i}_{\mu\nu} W_{i}^{\mu\nu} - \frac{1}{4} B_{\mu\nu} B^{\mu\nu} + \sum_{\psi} \bar{\psi} \gamma^{\mu} \left(i\partial_{\mu} - \frac{1}{2} g' Y_{\mathrm{W}} B_{\mu} - \frac{1}{2} g \sigma^{a} W^{a}_{\mu} \right) \psi,$$

where W^{i}_{μ} and B_{μ} are the four (i runs from 1 to 3) gauge fields of electroweak theory and $W^{i}_{\mu\nu}$ and $B_{\mu\nu}$ are their field strength tensors, the ψ sum is over all left–handed fermionic (lepton and quark) fields, γ_{μ} is the Dirac matrices, g and g' are the coupling strengths of the theory, Y_{W} is the weak hypercharge associated with the fermionic field and σ_{i} are the Pauli matrices. The terms for right–handed fermions,

$$\mathcal{L}_{EW,\,R} = \sum_{\psi_R} \bar{\psi}_R \gamma^{\mu} \left(i\partial_{\mu} - \frac{1}{2} g' Y_{W} B_{\mu} \right) \psi_R,$$

have been omitted for brevity.

The physical $W^{\pm}_{\mu}$, Z^{0}_{μ} and A_{μ} fields, which manifest as the $\mathrm{W}^{\pm}$ and Z^{0} bosons and the photon, respectively, arise as mixtures of the gauge fields:

$$\begin{aligned} W^{\pm}_{\mu} &= \frac{1}{\sqrt{2}} W^{1}_{\mu} \mp i W^{2}_{\mu} \\ Z^{0}_{\mu} &= W^{3}_{\mu} \cos\theta_{W} - B_{\mu} \sin\theta_{W} \\ A_{\mu} &= W^{3}_{\mu} \sin\theta_{W} + B_{\mu} \cos\theta_{W}, \end{aligned} \tag{2.5}$$

where θ_{W} is the Weinberg mixing angle, an empirically determined parameter of the model. It also relates the coupling strengths to the electromagnetic coupling constant e though

$$e = g' \cos\theta_{W} = g \sin\theta_{W}.$$

Applying the relations in eqs. (2.5) allows us to rewrite $\mathcal{L}_{EW}$ to a form that depends solely on these physical fields. Focusing on terms that depend on

$$F_{\mu\nu} = \partial_{\mu} A_{\nu} - \partial_{\nu} A_{\mu},$$

the electromagnetic field strength tensor, that come from just the first two terms in $\mathcal{L}_{EW}$, produces

$$\mathcal{L}_{EW} = -\frac{1}{4} F^{\mu\nu} F_{\mu\nu} + ie F^{\mu\nu} W^{+}_{\mu} W^{-}_{\nu} + \cdots \tag{2.6}$$

The first of these terms describes the propagation of the A_{μ} field from one configuration to another, or, in more immediate terms, the propagation of photons through space. Fourier–transforming to momentum space allows us to write the action for this term as

$$S_{EW} = -\frac{1}{2} \int \frac{d^{4}k}{(2\pi)^{4}} \tilde{A}_{\mu}(k) k^{2} \tilde{A}_{\nu}(-k) + \cdots, \tag{2.7}$$

implying that the photon propagator in momentum space is

$$\Delta(k) = \frac{1}{k^2 - i\epsilon}, \tag{2.8}$$

assuming that momentum conservation is imposed. Here, the modification of the denominator by $i\epsilon$ is included to avoid the pole at $k = 0$. Tilde denotes the Fourier transform of a field. This particular way of dealing with poles in the integration of the propagators is due to Richard Feynman, making this the Feynman propagator.

Similarly, the action associated with the second term in eq. (2.6) may be written as

$$S_{EW} = \cdots + ie \int_k (k_+ - k_-)\tilde{A}(k_A)\tilde{W}^+(k_+)\tilde{W}^-(k_-)\delta(k_A + k_+ + k_-) + \cdots, \tag{2.9}$$

where the integral is over all momenta, with measure $dk^4/(2\pi)^4$. The delta function ensures momentum conservation. We infer from this that an interaction exists between the A_μ and $W_\mu^\pm$ fields, weighted by a factor ie and a factor which, due to momentum conservation, depends on all three participating momenta.

Examining every term in the Lagrangian in this way, we may construct expressions that govern every process allowed by the Standard Model. Of note in relation to the search being carried out in this thesis, this list of processes does contain any vertices of the types AAA, AAZ, AZZ or ZZZ. Some of these neutral triple gauge couplings would clearly be able to produce two–photon final states, which would affect the result of the present search. Whether processes with two–photon final states that arise from these vertices exist is difficult to say, as no studies examining such processes have come to the authors attention. Certainly, the LHC has not produced any.

2.3 Feynman diagrams

Also due to Richard Feynman is the notion that the terms in the Lagrangian can be represented graphically.

We represent the photon propagator given in eq. (2.8) graphically as shown in fig. 2.1.

Figure 2.1: Feynman rule for the photon propagator.

The second term, from eq. (2.9), describes an interaction between the photon and the W bosons, the graphical representation of which is given in fig. 2.2. The associated factor has been simplified to omit dependencies on the external momenta.

The full propagators for the remaining fields require the introduction of the Higgs Lagrangian, which gives the mass terms for those fields. The relevant terms from the

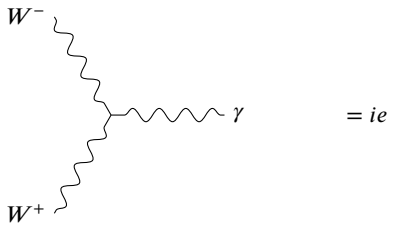

Figure 2.2:
Feynman rule for the $\gamma W^+ W^-$ coupling.

Higgs Lagrangian, in terms of physical fields, as given in eq. (2.5), are

$$\mathcal{L}_H = -\frac{g^2 v^2}{4} W^{+\mu} W^-_\mu - \frac{g^2 v^2}{8 \cos\theta_W} Z^\mu Z_\mu + \cdots, \tag{2.10}$$

where $v/\sqrt{2}$ is the vacuum expectation value of the Higgs field, given the correct Gauge transformation. From this, we identify the mass terms

$$m_W = \frac{g^2 v^2}{2}, \qquad m_Z = m_W \cos\theta_W. \tag{2.11}$$

Including the mass terms in the action for, say, a free Z^0 boson and Fourier–transforming gives us

$$S_Z = \int \frac{d^4k}{(2\pi)^4} \tilde{Z}_\mu(k)[k^2 - m^2]\tilde{Z}\nu(-k)) + \cdots,$$

leading to the bosonic Feynman propagator,

$$\Delta(k) = \frac{1}{k^2 - m^2 - i\epsilon}, \tag{2.12}$$

which is the factor associated with the propagators for the remaining electroweak bosons, and the Higgs propagator, which are drawn as shown in figure 2.3, along with the gluon propagator produced by $\mathcal{L}_{QCD}$, for completeness. As this is merely an overview, we do not include the associated factors. A complete listing can be found in [4].

Figure 2.3:
Showing how line shapes and SM particles are associated.

In fig. 2.3, the notion that antiparticles are time–reversed particles is introduced, as indicated by the direction of the arrows.

The remainder of $\mathcal{L}_{EW}$ gives rise to couplings of the types shown in fig. 2.4. For brevity, we do not show a complete listing of Feynman rules, only a condensed overview of possible vertices. For a complete listing, see eg. [4]. The couplings introduced by the QCD and Higgs sectors are given in figure 2.7.

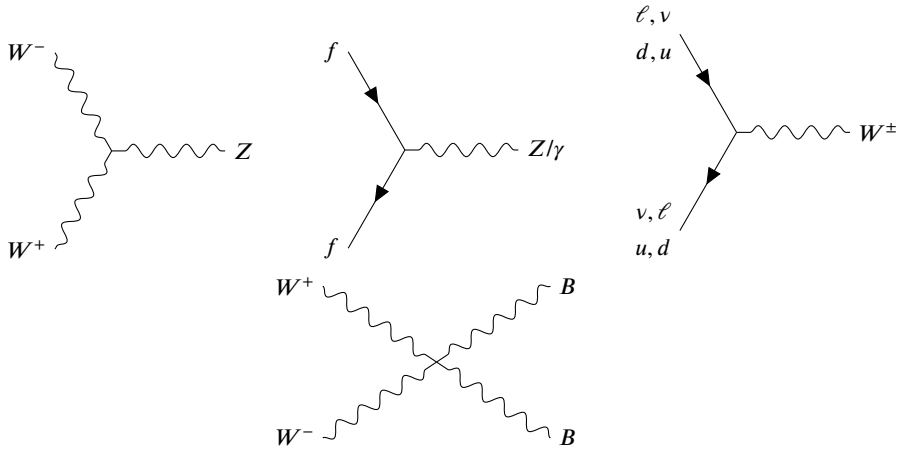

Figure 2.4:
The Feynman rules of the electroweak Lagrangian, excluding those given in figures 2.1 and 2.2. Here, B may be any electroweak boson (γ, Z^0 or $W^\pm$, so long as charge is conserved. f is any fermion, respecting that photons only couple to electrically charged fermions and ℓ, ν, u, d are lepton–neutrino or up–type—down–type quark sets.

An advantage of representing the terms of the Lagrangian in this way is that it allows an easy identification and organisation of possible processes, and subsequently deduction of the action that governs the associated transition amplitude. This is because Feynman diagrams are required to conserve momentum and quantum numbers, and each of the elements of a Feynman diagram are directly associated with an element of the governing equation through Feynman rules, such as were given in fig. 2.1 and 2.2.

For example, with the $f\bar{f} \to \gamma$ and the q propagator already introduced, we may assemble the Feynman diagram in fig. 2.5 for a $q\bar{q} \to \gamma\gamma$ process.

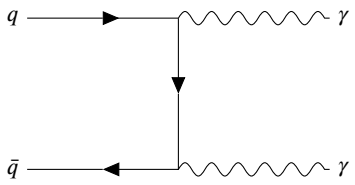

Figure 2.5:
A Feynman diagram for a $q\bar{q} \to \gamma\gamma$ process.

To evaluate this diagram, we require the Feynman rule for the $f\bar{f} \to \gamma$ vertex, given in fig. 2.6

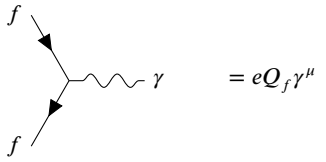

Figure 2.6:
Feynman rule for the fermion–fermion–photon coupling. e is the unit charge and Q_f is the charge of the fermion.

The Feynman diagram in fig. 2.5 is then equivalent to

$$e^2 Q_q^2 \gamma^\mu \gamma^\nu \frac{i(\not{k} + m)}{k^2 - m^2 - i\epsilon}, \tag{2.13}$$

where the faction is the quark propagator. This relates to the action by integrating over all participating momenta, keeping in mind that momenta must be conserved across all propagators and in every vertex.

The Feynman rules introduced by the QCD and Higgs sectors are indicated in figure 2.7.

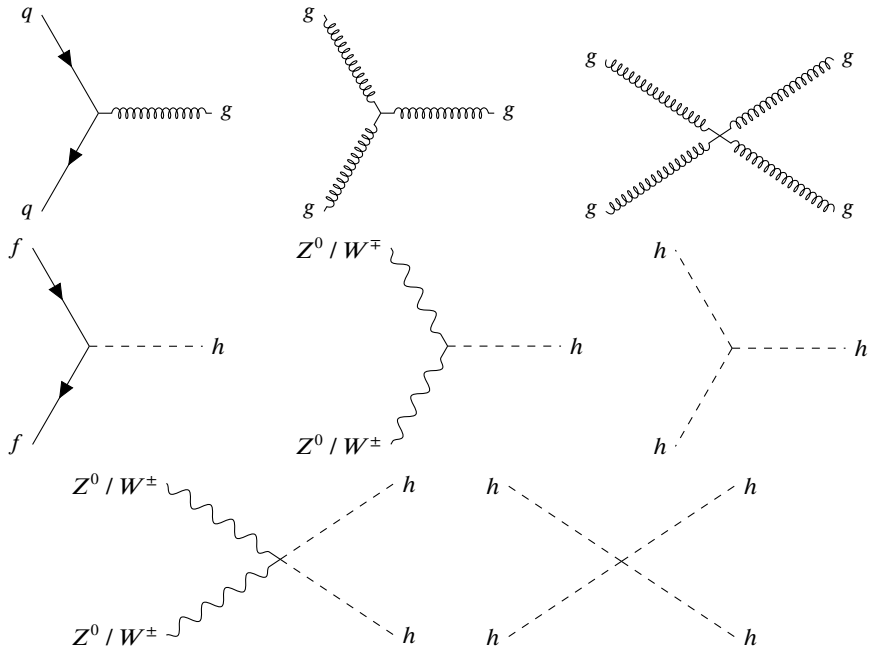

Figure 2.7:
Couplings introduced in $\mathcal{L}_{QCD}$ and $\mathcal{L}_H$.

With these couplings in the mix, we can additionally construct the diagrams with $\gamma\gamma$ final states in figure 2.8.

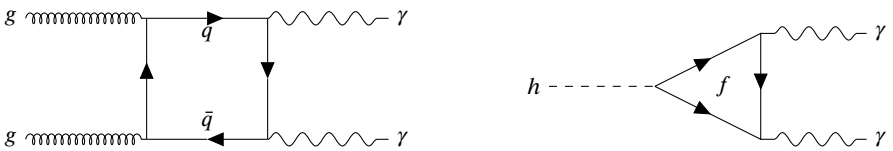

Figure 2.8:
Single loop level Feynman diagrams with $\gamma\gamma$ final states.

Both these diagrams introduce a new complication, in that the internal loops contain a momentum which is not fixed by momentum conservation in the vertices to

external momenta. Thus, the momentum integration on this diagram will diverge. There exist well defined procedures for renormalising the contributions from these loop level diagrams, however, as this requires the development of next–to–leading order methods, we will consider them beyond our scope. We will in any case not be calculating contributions from higher than leading order diagrams directly.

The rightmost diagram in fig. 2.8 is one of the decay modes of the Higgs boson. As such, the invariant masses of the resulting photon pair will tend to distribute itself around the Higgs boson mass. In fact, this process was one of the main areas of focus in the recent search for the Higgs boson. This distribution of invariant masses, we will see in the following, is quite different from the signature of the event that are the subject of the present search. Thus, the contribution from this diagram will not figure in the analysis to follow.

The procedure outlined above, for constructing a collection of Feynman diagrams from a Lagrangian can be described in sufficient detail to be automated. For this thesis, we will use the tool LanHEP [5] for this purpose. This tool is chosen for its easy compatibility with the event generator which will be used in chapter 3. Alternatives exist, such as FeynRules [6].

We will now extend the Standard Model to encompass an additional $qq \to \gamma\gamma$ process via the effective Lagrangian approach.

2.4 The effective Lagrangian approach

The SM Lagrangian can be written as a sum of terms, each of which describes the behaviour of or interactions between the fields in the Standard Model [3], as we also exploited above, to write it in terms of Feynman diagrams. It is no great stretch, then, to consider expanding the Standard Model by adding a new term to the Lagrangian, which describes some new physics. Doing so, however, is not unproblematic.

It is a property of the Standard Model that it is unitary, meaning that the total probability of a given state to propagate into any of the possible final states evaluates to 1. Clearly, one cannot simply add any new term to the Standard Model Lagrangian without breaking this unitarity. Rather than going through the painstaking process of ensuring that the new term we will add to the SM preserves its unitarity, we will in stead build on the assumption that new physics exists at high mass scales, and think of the SM Lagrangian as simply the zeroth order term in a series expansion of some larger model. There will then be higher order corrections to the Standard Model, in some mass scale Λ that the expansion is performed in. In that case, the SM is no longer assumed to be a complete model, and, moreover, the expanded model is not even expected to be a complete model to any given order in Λ, which allows us to sidestep the issue of unitarity. We can only do this if the mass scale Λ is significantly higher than the energies at which the Standard Model is being probed. By assuming that the Standard Model is a zeroth order term in a larger model, we require that its parameters are determined in an energy range free of the effects of any higher order terms.

From this assumed plethora of possible higher order terms, we choose to consider a specific term, which describes the $q\bar{q} \to \gamma\gamma$ contact interaction which is the focus of this thesis. This term takes the form [7]

$$\mathcal{L}_n = \frac{2ie^2}{\Lambda^4} Q_q^2 F^{\mu\sigma} F_\sigma^\nu \overline{q} \gamma_\mu \partial_\nu q, \tag{2.14}$$

where e is the elementary charge, Q_q is the quark charge of quark q and Λ, as discussed, is the associated mass scale. n is for "new". The power of Λ is chosen to give the correct mass dimension of the term: in natural units,[2] the action is unitless. The Lagrangian is integrated over 4 lengths to give the action, which means it must have a length dimension of -4 itself. Finally, in natural units, we can equate a unit of length with a unit of inverse mass[3], which means that the Lagrangian must have mass dimension 4. The factors $F^{\mu\sigma} F_\sigma^\nu$ and $\overline{q}\gamma_\mu \partial_\nu q$ each contribute a mass dimension of 4, so the mass scale Λ (which has dimension of mass) must get a power of -4.

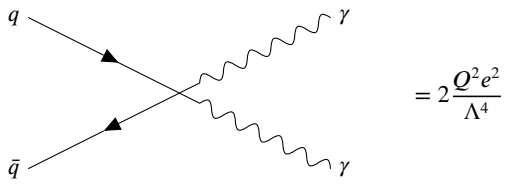

Figure 2.9:
The Feynman rule created by entering the new term from eq. (2.14) into LanHEP[5]. As we are assuming that Feynman diagrams always must conserve momentum and quantum numbers, several trivial δ-functions have been omitted.

The effect of the new term is to introduce the Feynman rule shown in fig. 2.9.

One possible interpretation of this new four-point interaction is as a zero-range approximation of a process like the one shown in fig. 2.10(b), involving some unknown mediating particle with mass approximately equal to Λ [8]. The proposed graviton is one candidate for such a particle.

2.5 The cross section

Using the methods developed so far, we can calculate the transition amplitudes, and hence the probabilities, associated with a single processes. However, by long standing tradition, particle physics is interested in the cross section σ.

[2] Where $\hbar = c = 1$.

[3] Because in natural units,

$$[\text{length}] = [\text{length}]\frac{c}{\hbar} = [\text{length}]\frac{\left[\frac{\text{length}}{\text{time}}\right]}{\left[\frac{\text{length}^2\ \text{mass}}{\text{time}}\right]} = \left[\frac{\text{length}^2\ \text{time}}{\text{length}^2\ \text{time mass}}\right] = [\text{mass}]^{-1}.$$

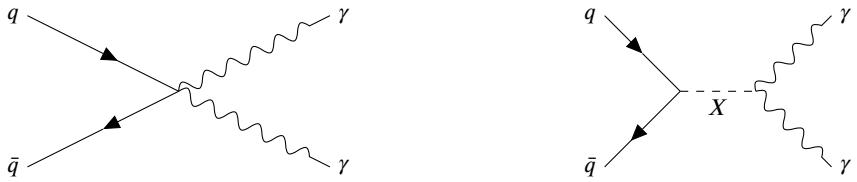

(a) Point $q\bar{q}\gamma\gamma$ interaction.

(b) The $q\bar{q}\gamma\gamma$ interaction with mediating particle X.

Figure 2.10:
Feynman diagrams of the relevant contact interaction. (a) is the interaction described by the new term in the Lagrangian, while (b) is the type of interaction this can be considered a zero-range approximation of.

The relationship between a probability and a cross section follows from considering the case where a single projectile is fired at a single target. We might at this point imagine an arrow and a bulls-eye or an electron and an atomic nucleus in a piece of gold film [9]. The probability of hitting the target is then the cross sectional area of the target σ divided by the cross sectional area A of the space where the projectile might fly. Adding the possibility of a number, N_P, of projectiles being fired at a number, N_T, of different, non-overlapping targets, the number, N, of hits is calculated as

$$N = \frac{N_P N_T \sigma}{A}.$$

If we apply this picture to a quantum mechanical system, we are mixing the kinematic probability for two particles coming close enough to interact with the dynamic probability of a particular interaction occurring. We can fix this by expressing the probability $\mathcal{P}$ as a function of the separation between the interacting particles, given by the impact parameter $\mathbf{b}$, a 2D vector, and then integrating over all $\mathbf{b}$. Then, we can write

$$\sigma = \int d^2b\, \mathcal{P}(\mathbf{b}) \propto \mathcal{P}(\text{in} \to \text{out}) = |A(\text{in} \to \text{out})|^2 .$$

The transition amplitude $A(\text{in} \to \text{out})$, in this context, is the transition amplitude, defined in eq. (2.4), derived from the action for the process being studied. In this way, we can calculate the cross section of some process from its transition amplitude.

2.6 Parametrisation of the contact interaction

Since the new contact interaction has been introduced by adding a term to the SM Lagrangian, we may, due to eq. (2.3), write the transition amplitude for the $qq \to \gamma\gamma$ processes as

$$A(qq \to \gamma\gamma) = \int \mathcal{D}\phi e^{i(S_{SM}[\phi]+S_n[\phi])}, \tag{2.15}$$

where S_{SM} is the action associated with the Standard Model Lagrangian and S_n is the action that arises from the new term $\mathcal{L}_n$. Through a series expansion, this can be written as

$$A(qq \to \gamma\gamma) = \int \mathcal{D}\phi e^{iS_{SM}} \left(1 - iS_n + \frac{(-iS_n)^2}{2} + \cdots\right) = \int \mathcal{D}\phi e^{iS_{SM}} + \int \mathcal{D}\phi N_n, \tag{2.16}$$

where we defined

$$N_n = e^{iS_{SM}} \left(-iS_n + \frac{(-iS_n)^2}{2} + \cdots\right). \tag{2.17}$$

Combining eqs. (2.3) and (2.14), we find that N_n may be written as

$$N_n = e^{iS_{SM}} \left(-i \int \frac{dk^4}{(2\pi)^4} \frac{2ie^2}{\Lambda^4} Q_q^2 F^{\mu\sigma} F_\sigma^\nu \overline{q} \gamma_\mu \partial_\nu q + \frac{1}{2}\left[-i \int \frac{dk^4}{(2\pi)^4} \frac{2ie^2}{\Lambda^4} Q_q^2 F^{\mu\sigma} F_\sigma^\nu \overline{q} \gamma_\mu \partial_\nu q\right]^2 + \cdots\right), \tag{2.18}$$

which is an expression proportional to Λ^{-4}.

Making the proportionality explicit by defining

$$\mathcal{M}_{SM} = \int \mathcal{D}\phi e^{iS_{SM}} \qquad \text{and} \qquad \frac{1}{\Lambda^4}\mathcal{M}_n = \int \mathcal{D}\phi N_n, \tag{2.19}$$

we may write the transition probability

$$\begin{aligned} \mathcal{P}(qq \to \gamma\gamma) &= |A(qq \to \gamma\gamma)|^2 \\ &= \left|\mathcal{M}_{SM} + \frac{1}{\Lambda^4}\mathcal{M}_n\right|^2 \\ &= \mathcal{M}_{SM}^2 + \frac{2}{\Lambda^4}\mathrm{Re}[\mathcal{M}_{SM}\mathcal{M}_n] + \frac{1}{\Lambda^8}\mathcal{M}_n^2. \end{aligned} \tag{2.20}$$

This is a second order polynomial in Λ^{-4},

$$\mathcal{P}(qq \to \gamma\gamma) = a + b\frac{1}{\Lambda^4} + c\left(\frac{1}{\Lambda^4}\right)^2. \tag{2.21}$$

In the following, we shall develop a procedure for determining the cross section of the $qq \to \gamma\gamma$ process for given values of Λ. As we just saw, however, the Λ dependence of the cross section is given by the polynomial in equation (2.21). Thus, if we have the cross section at three values of Λ, we can determine the value of the coefficients a, b and c, and with those, we may calculate the cross section for the process at any value of Λ. Determining the coefficients by that route, we need not even concern ourselves with the content of those coefficients, although it remains clear that the a coefficient is identical to the Standard Model cross section for the process.

2.7 Considering protons

In the processes described so far, the starting point has been the interaction of a quark and an antiquark. And while being able to single out such a process experimentally would certainly be nice, single quarks sadly do not occur in nature. Because quarks are colour charged particles, they are subject a phenomenon known as colour confinement, which requires that colour charge always occur in bundles which are colour neutral when viewed from the outside. For our purposes, protons are an abundant, stable and easy–to–handle colour–neutral bundle of quarks and gluons, which we use in collisions in place of the naked quarks that would have been optimal for the present analysis.

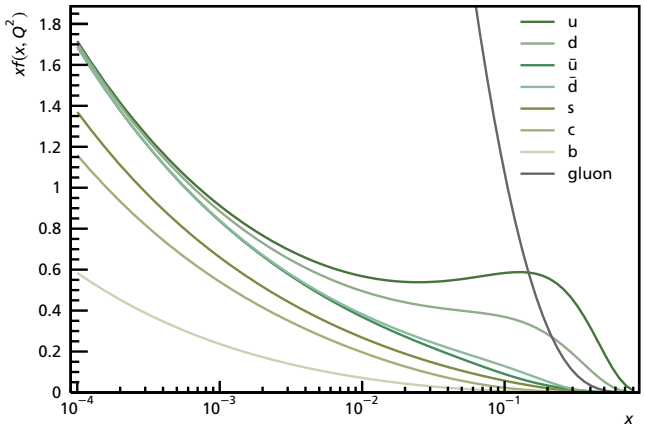

Figure 2.11: Parton distribution function obtained from the CTEQ collaboration. It expresses the probability of extracting a specific quark from a proton with a certain fraction, x, of its energy as a function of x and Q^2. This illustration has $Q^2 = 100$ GeV^2. Adapted from [10].

While protons contain no antiquarks as valence quarks, every proton also contains a 'sea' of virtual particles. At a given energy scale Q^2, there is a certain probability for extracting one of these sea quarks (or gluons) with a fraction x of the kinetic energy of the proton in an interaction. This probability is given by the Parton Distribution Functions (PDFs), a selection of which is shown in fig. 2.11. These functions are found experimentally by several collaborations. This thesis will deal mainly with the CTEQ set of PDFs.

Including this step in the calculation leads to the following expression, which gives the cross section for a diphoton event resulting from a proton-proton collision, $\sigma(pp \to \gamma\gamma)$ in terms of the $\sigma(q\bar{q} \to \gamma\gamma)$ cross section that we have determined thus far:

$$\sigma(pp \to \gamma\gamma) = \sum_q \iint dx_1\, dx_2\, f_q(x_1, Q^2) f_{\bar{q}}(x_2, Q^2) \sigma(q\bar{q} \to \gamma\gamma),$$

where f_q is the PDF for parton q.

2.8 Interference with the Standard Model

These new processes that arise from eq. (2.14) may interfere constructively or destructively with the Standard Model contributions to this process.

To examine the effects of both, we define a convenient variable for examining distributions of diphoton events, the invariant mass $M_{\gamma\gamma}$, as [11]

$$M_{\gamma\gamma} = \sqrt{(E_1 + E_2)^2 - |\mathbf{p}_1 + \mathbf{p}_2|^2},$$

which, in the case of massless particles, can be rewritten as

$$= \sqrt{2p_1p_2(1 - \cos\theta)}$$

Figure 2.12 presents a distribution in invariant mass of events produced both when assuming constructive and destructive interference.

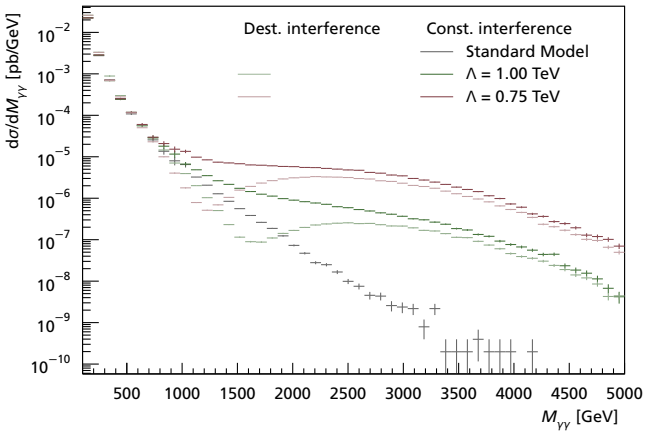

Figure 2.12:
The effect on the distribution of the invariant masses of the produced photon pairs of introducing the new term into the Lagrangian at various values of the mass scale Λ, assuming constructive (non-grayed) and destructive (grayed) interference with the SM contribution. Note that the distributions that assume destructive interference produce fewer events than those that assume constructive interference at the same value of Λ. These Monte Carlo samples were produced with CalcHEP [12].

As should be evident from this figure, a sample of events produced when assuming constructive interference contains more events at every point than a sample produced if assuming destructive interference at the same value for Λ. Recalling eq. (2.21), this difference in behaviour is reproduced by changing the sign of the linear, b, coefficient. Thus, a parametrisation carried out on the basis of a distribution that assumes either kind of interference can still recreate distributions that exhibit the behaviour of the other type of interference, simply by reversing the sign of b. Thus, we loose no information by considering only constructive interference in the following.

3 Simulation studies

Now that the theoretical description of the processes under study is in place, we might suppose that obtaining a prediction of the distributions of events that an experiment will find is a simple matter of carrying out the integrals laid out in the previous chapter. Unfortunately, these integrals defy analytical solution, which leaves only the option of integrating numerically. Specifically, we will use the Monte Carlo method for numerical integration, which prescribes inserting a random value drawn from a suitable distribution into the integrand in place of the variable of integration, and then calculating the value of the integrand. Each result estimates the value of the integral, and by averaging several such estimates, an incrementally better estimate is obtained.

Since all of the variables that are integrated over have physical significance, choosing specific values for the variables of integration can be viewed as equivalent to laying out the kinematics of a single hypothetical event. Repeatedly estimating the value of the integral a sufficient number of times to obtain a result of acceptable accuracy from the Monte Carlo integration process in effect leaves us with a large set of such simulated events. In particle physics, this process goes by Monte Carlo simulation, and the software packages that are designed to carry out these calculations are called event generators.

3.1 Event generators

The event generator used for the bulk of the work in this thesis is CalcHEP [12].

Given a set of initial and final states and a list of Feynman rules, CalcHEP can construct all tree level diagrams that contribute to the specified process. By specifying a composite particle, such as a proton, CalcHEP will construct Feynman diagrams with initial states composed of any combination of particles that can be extracted from the given composite, weighted by a selected PDF. For generating our event samples, we specify protons with 4 TeV momentum in the initial state and two photons in the final state. Based on the collection of Feynman diagrams thus constructed, CalcHEP can then generate events according to those Feynman diagrams, in the correct proportions.

Other choices of event generators include MadGraph [13] and pythia [14]. To illustrate the behaviour of these different generators with respect to one another, figure 3.1 plots distributions of invariant mass ($M_{\gamma\gamma}$) and transverse momentum (p_T) of a set of simulated events generated by each one. To accurately compare the three, all are limited to tree level processes, to conform to the limitations of CalcHEP.

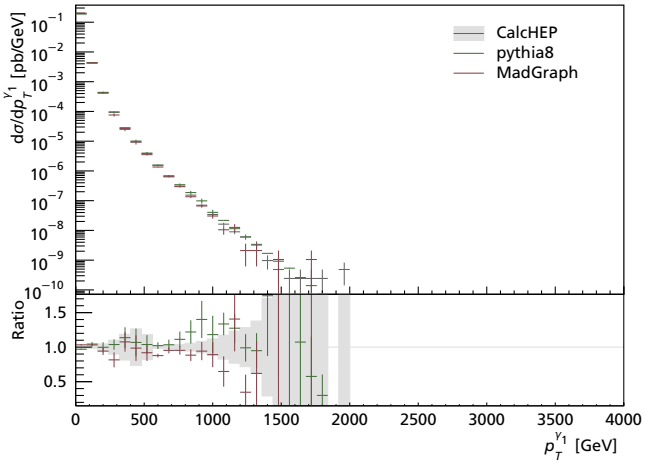

(a) The distribution of $p_T^{\gamma_1}$, the transverse momentum of the leading photon, in the event samples produced by three event generators.

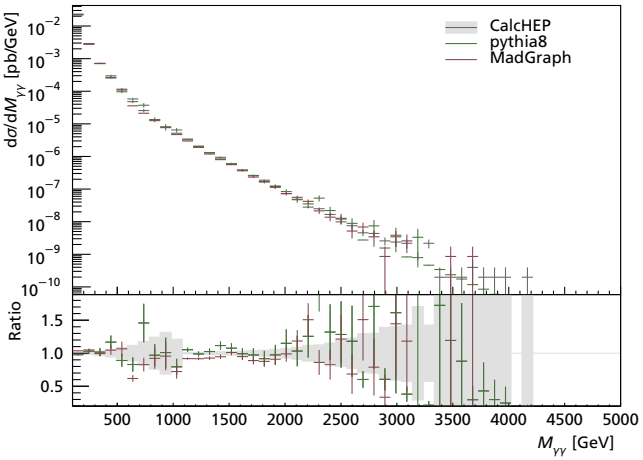

(b) The distribution of $M_{\gamma\gamma}$, the invariant mass of the photon pair, in the event samples produced by three event generators.

Figure 3.1:
Plots showing the distributions of p_T and $M_{\gamma\gamma}$ of events generated by the three event generators [12, 14, 13]. Below, the ratio plots were created by dividing the content in each bin of the distributions with the content of the corresponding bin in the distribution for the CalcHEP sample. The errors on the bins were derived through standard error propagation. All these samples were produced using stratified sampling, where separate sets of events were produced for different ranges of p_T, as discussed in the text.

These plots, and those to follow in this chapter, have at some stage of their creation been through the analysis validation software RIVET[1] [15].

The strong coupling constant, α_S, is a so–called running coupling constant [11], meaning that its value changes depending on an energy scale, Q, at which it is examined. How this energy scale is determined is defined differently by default in CalcHEP than it is in pythia and MadGraph. To achieve the result in figure 3.1, this setting in CalcHEP was changed to

$$Q^2 = \frac{p_T(\gamma_1)^2 + p_T(\gamma_2)^2}{2},$$

which is the setting used in the other two event generators.

As figure 3.1 illustrates, there is a difference of 8–9 orders of magnitude between the number of events produced in the low and the high p_T ranges. Covering this entire range requires more simulated events than we can feasibly analyse. To circumvent this issue, we employ stratified sampling, meaning that we create several smaller samples that cover successive ranges in a representative variable. In this case, we create four sets of events to cover the following ranges in $M_{\gamma\gamma}$:

1. $M_{\gamma\gamma} \in [0; 100)$ GeV
2. $M_{\gamma\gamma} \in [100; 420)$ GeV
3. $M_{\gamma\gamma} \in [420; 1000)$ GeV
4. $M_{\gamma\gamma} \in [1000; \infty)$ GeV

In fig 3.1, one easily noticeable effect of this stratification of event samples is the jump in statistical uncertainties around 500 GeV in p_T or 1 000 GeV in $M_{\gamma\gamma}$.

In addition, the fiducial volume for the event sample is bounded by a minimum requirement of 50 GeV in E_T and a maximum of 2.5 in $|\eta|$.

The event samples generated by CalcHEP and pythia are compatible with one another in both these distributions, however, the sample generated by MadGraph seems to produce fewer events with an invariant mass between 1 000 and 2 000 GeV compared to the other samples. This sample was not produced by the author, which makes investigation into the cause of this bias difficult. For the present analysis, the bias is included as a systematic uncertainty of 9.18% on the overall normalisation arising from the choice of event generator, however it remains a possibility that this uncertainty could be reduced or eliminated by a more careful study.

3.2 Discriminating variables

To allow CalcHEP to generate events that involve the new contact interaction, we can simply extend the list of Feynman rules known to CalcHEP to include the new

[1] **R**obust **I**ndependent **V**alidation of **E**xperiment and **T**heory.

Feynman rule we found in chapter 2, using LanHEP [5]. In practice, this involves giving as input a Lagrangian written in a format similar to LaTeX's math language. LanHEP then produces a list of Feynman rules in a format appropriate for CalcHEP. This new model has two additional parameters: the size of Λ and the sign of the interference of this new interaction with the existing processes.

With the ability to produce sets of events with varying values of Λ, the opportunity presents itself to create simulated distributions of events for several potential observables that we might examine to discriminate the effects of the contact interaction. To quantify the discriminating power of these observables, we define a figure of merit, which we will call 'significance', as

$$S \equiv \frac{1}{N} \sum_n \frac{|x_n - y_n|}{\sqrt{{\sigma_{x,n}}^2 + {\sigma_{y,n}}^2}}, \tag{3.1}$$

where the sum is over bins n where both distributions have non–zero content, N is the total number of bins where both distributions have non–zero content, x_n and y_n are the content of the two distributions in bin n, and $\sigma_{x,n}$ and $\sigma_{y,n}$ are the uncertainties on the bin content of each of the two distributions in bin n. Results for a few selected variables are shown in figure 3.2.

Given the significances quoted in that figure, $p_T^{\gamma_1}$, the transverse momentum of the leading photon, is the obvious choice for a discriminating variable. It, along with the scattering angle, has the disadvantage when compared with the latter two methods, however, that it is dependant on identifying the leading—most energetic—photon of the pair. In a truth sample such as this, making such an identification does not present a problem, however when considering the effects on a photon of passing through the material of the detector, it becomes problematic to claim that the photon that leaves the largest energy deposit in the calorimeter is also the photon that left the hard event with the greatest amount of energy. The two remaining variables both incorporate information about both photons. The invariant mass additionally incorporates information about the relative orientation of the photons, which arguably makes it the most sophisticated measure.

For this reason, we will use invariant mass as the discriminating variable going forward.

Meanwhile, figure 3.2(a) shows no discernible difference between the SM sample and the sample generated with a 1 TeV mass scale contact interaction. Evidently, at the hard process level, the distribution of angles between photons is not affected by the new term.

3.3 Parton Distribution Functions

As described in section 2.7, we use a set of experimentally determined functions called Parton Distribution Functions (PDFs) to describe the probability of extracting a given parton from a proton. Given that the PDFs are not exact analytical models, we must account for the uncertainty associated with the method by which PDFs are determined.

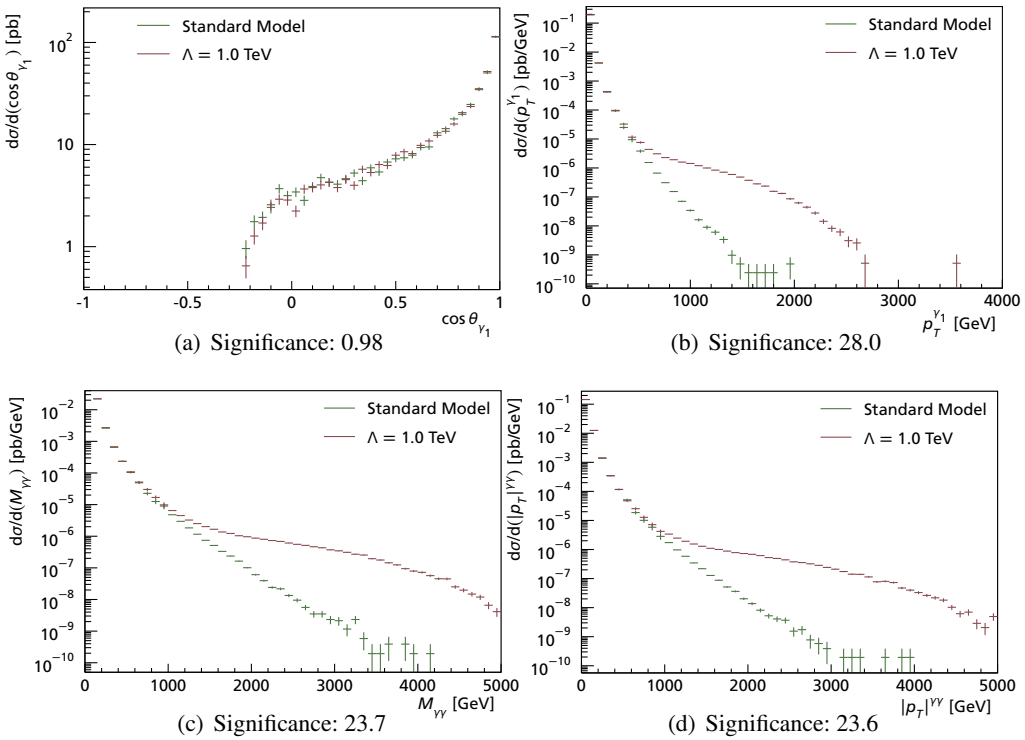

(a) Significance: 0.98 (b) Significance: 28.0

(c) Significance: 23.7 (d) Significance: 23.6

Figure 3.2:
The distributions of simulated events in four potential discriminating variables in event samples generated with Standard Model parameters, and with $\Lambda = 1.0$ TeV: (a) the cosine of θ_{γ_1}, the scattering angle of the leading photon (measured, in this case, in the Collins-Soper frame [16]), (b) $p_T^{\gamma_1}$, the transverse momentum of the leading (most energetic) photon, (c) $M_{\gamma\gamma}$, the invariant mass of the photon pair and (d) $|p_T|^{\gamma\gamma}$, the sum of magnitudes of p_T of both photons. Both samples are generated with CalcHEP. The significance is calculated according to eq. (3.1).

To estimate that uncertainty, we compare the distribution in invariant masses of events generated by CalcHEP using the CTEQ6 set of PDFs, which are the events that will be used moving forward, with events generated using the alternative MRST2002nlo set of PDF, which is the only alternative PDF available in CalcHEP.

The resulting distributions are plotted in fig 3.3, and the difference between the sample generated using the CTEQ6 PDF set and the MRST2002 PDF set are quantified in table 3.1, broken up into three invariant mass ranges: a low range with a great deal of statistics and very little separation between the three models, a middle range with good statistics and good separation between the models, and a high range where statistics start to run out, especially for the SM sample. Additionally, as we will return to in chapter 5, the data sample runs out of statistics below 2 TeV. Looking at the ratio plots in figure 3.3, we must conclude that the predictions produced by the to PDFs differ in a non–trivial way, which depends on Λ. These deviations must be included in the analysis as a systematic uncertainty.

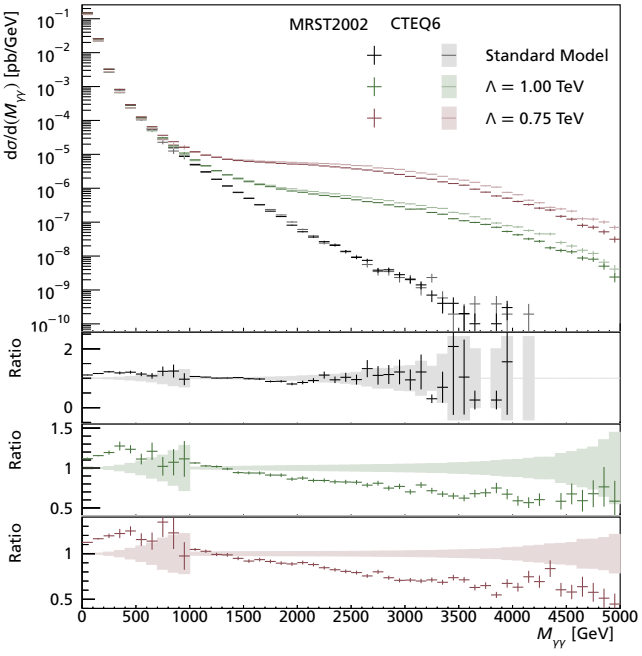

Figure 3.3:
Comparing the distribution of invariant masses of events produced by CalcHEP with the CTEQ6 (grayed) and MRST2002nlo (non–grayed) PDFs at different values of Λ, along with a ratio plot showing the differences between the distributions at each value of Λ. This is to give an idea of the systematic uncertainty on this distribution due to the choice of PDF. Table 3.1 summarises the fractional variation in predicted events by Λ and invariant mass range. The invariant mass ranges used are discussed in the text.

		$M_{\gamma\gamma}$ range [GeV]		
		[100:1000)	**[1000:3000)**	**[3000:5000)**
Λ [TeV]	**0.75**	(13.1 ± 0.4) %	(11.7 ± 0.5) %	(31.9 ± 1.2) %
	1.00	(12.4 ± 1.0) %	(8.1 ± 0.5) %	(32.1 ± 1.7) %
	∞	(12.0 ± 1.0) %	(3.1 ± 0.6) %	(56 ± 21) %

Table 3.1:
The fractional deviation between the distribution of simulated events produced by CalcHEP with the CTEQ6 PDF versus the MSRT2002nlo PDF plotted in fig 3.3. We use a Λ value of ∞ as shorthand for the SM case, since inserting ∞ in Λs place in eq. (2.14) causes the new term to equal zero. The errors are derived from the statistical errors in those distributions. This will form one of the systematic uncertainties on the final result. Note in regards to the lower right number that the presence of zero–value bins in this part of the distributions may skew the error too low. The lesson here is that while the two PDFs agree reasonably well on the Standard Model prediction, they produce significantly diverging results when the new interaction term is introduced.

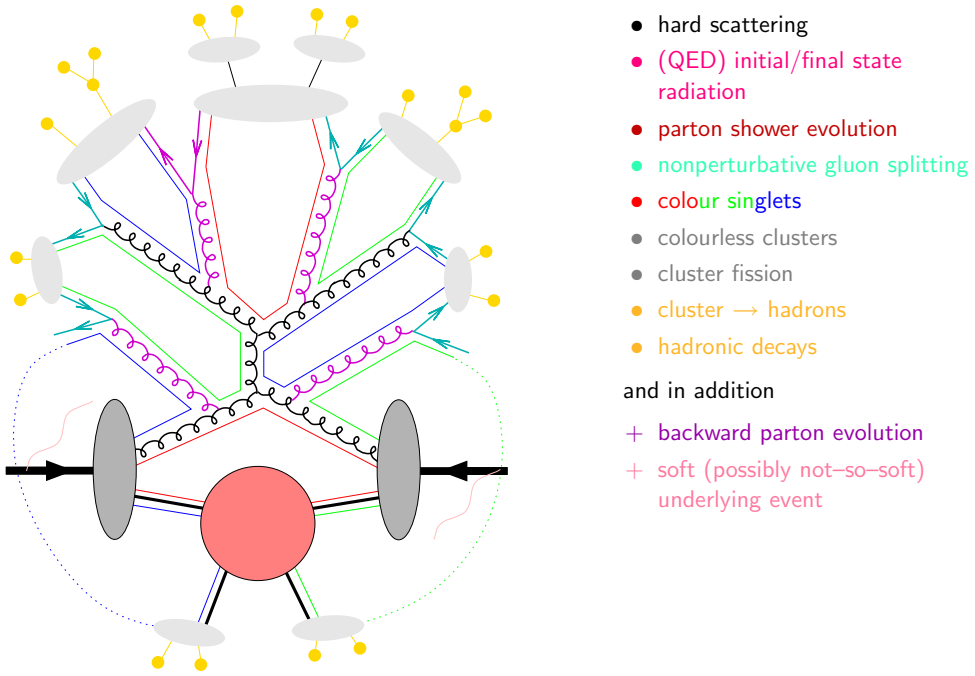

Figure 3.4:
An illustration of the processes that may surround an interesting event in a proton-proton collision, and the steps required to arrive at a final particle content of that event. In this figure, the dark gray blobs represent the incoming protons and the large red blob represents a hard quark-quark interaction. This figure reproduced from [17]. For further details on these surrounding processes and their computational representation, see e.g. [18].

3.4 Parton level effects

The events produced by the event generator(s) represent the hard physical process that occurs in the point where two protons interact. Given that we cannot observe such interactions at the moment they occur, and physics continues both before and after the hard event, we need to expand the scope of physical processes in the simulation, to the point where the resulting event information represents something that we might realistically observe with a detector.

Figure 3.4 gives a schematic overview of the processes that might occur in a proton interaction in addition to the hard process—the red blob—along with a list of steps that a simulation of these processes typically goes through.

Initial and final state radiation are of particular importance in the present analysis, since these can directly produce photons, which might enter into our signal reconstruction.

Figure 3.4 also illustrates how we might see more than one interaction between the constituents of interacting protons. In this case, several additional gluons are emitted.

Final state particles with colour charge, such as gluons, will not remain isolated

due to colour confinement. These particles will develop a jet of other coloured particles about themselves, so that the colour charge is neutralised to outside observation. The simulation of the process by which colour charged particles combine into colour neutral hadrons is simulated is called hadronisation. This simulates how a single coloured particle evolves into several colour–neutral hadrons in the space between the interaction point and the detectors. Due to the kinematics involved, the hadrons produced by a single particle will remain close enough together that the detector can not distinguish the individual particles from one another. We refer to such an object as a jet. Since we are dealing with photons in the final state in the present analysis, this step is not crucial in the events generated to study this process specifically, however π^0 mesons, one of the major backgrounds to the photon signal, are produced in this way.

In this thesis, the extension of the hard events provided by CalcHEP with these surrounding processes will be carried out in pythia8 [14]. Figure 3.5 illustrates the effect that these surrounding processes have on the distribution of invariant masses.

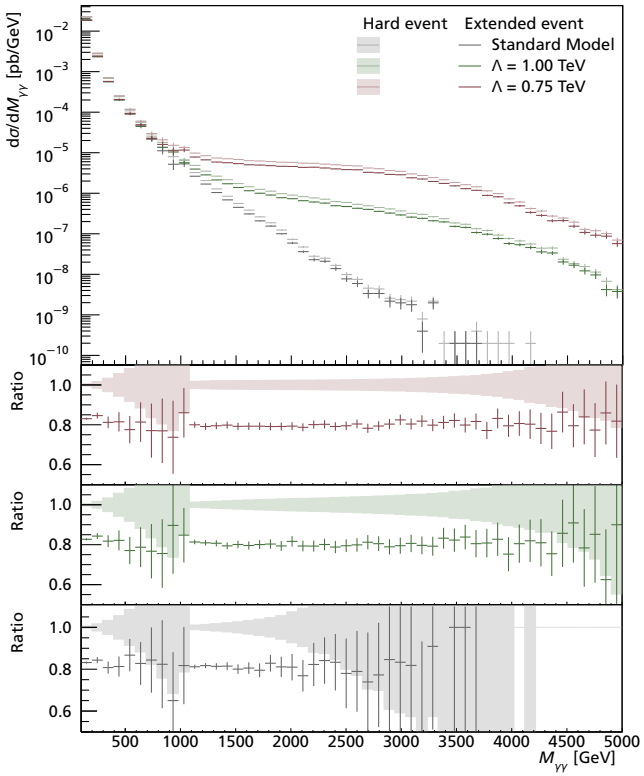

Figure 3.5:
The distribution of invariant masses in the event samples generated by CalcHEP at three values of Λ, and the same event samples after extending them in surrounding processes with pythia, with ratio plots. Once again, the effect of the use of stratified sampling is visible as a jump in the magnitude of the errors around 1000 GeV.

Here, the ratio plots make it clear that the effect upon this particular observable

of overlaying parton level effects is simply to remove a fraction of the events. This is reasonable, since the effect of adding final state radiation to a hard event is to alter the final state particle content for a fraction of those events, and since we require two final state photons to calculate an invariant mass, final states that do not contain two photons are discarded in the RIVET analysis step. We can conclude from this figure that the selection of events with altered final state particle content does not depend on the invariant mass of the photons in the event, nor does the process of overlaying parton level effects alter the distribution of photon invariant masses.

This constant difference in distributions between the process level and parton level event samples does not apply for all observables. Figure 3.6 illustrates how the distribution of $\cos\theta_{\gamma_1}$, the scattering angle for the leading photon is skewed slightly toward lower values, meaning a greater proportion of large scattering angles. This could be an effect of extended events having their kinematics altered so that the leading photon in the extended event is not the same as the leading photon in the hard event, so that the subleading photon, which scatter in the opposite direction from the leading photon, spill into the leading photon sample. This would also explain why the shape of the invariant mass distribution, which is not sensitive to the identification of a leading photon, is not affected.

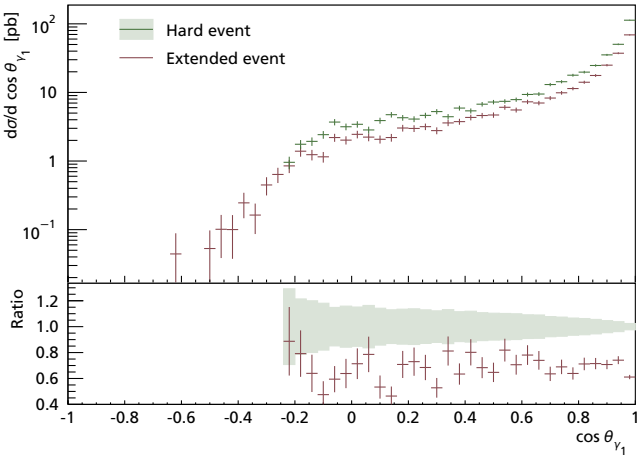

Figure 3.6:
A plot of the distribution of the cosine of the scattering angle θ (in the CS frame, as in fig. 3.2) of the leading photon in the set of events generated by CalcHEP in the SM scenario before (green) and after (red) being extended with pythia. Aside from the same constant faction of lost events as was also seen in fig. 3.5, we note that the distribution contains events with lower $\cos\theta_{\gamma_1}$ than were present in the set of generated events.

Since the main process under study does not involve coloured final states, we do not expect that these surrounding processes will be a significant source of systematic uncertainty or bias, We are supported in this assumption by the findings in figure 3.5. To support that expectation beyond what is done here, one might attempt to add the extended processes with a different software package.

4 Experiment

Having thus formed a clear picture of what observable effects we expect to manifest from our changes to the Standard Model, we can now proceed with the experimental test.

As was perhaps given away by the title, this thesis will use the already established ATLAS[1] experiment, which is part of the Large Hadron Collider complex at CERN[2] in Geneva.

4.1 The Large Hadron Collider

The CERN accelerator complex comprises a number of particle accelerators with a wide variety of sizes, which service several experiments with various aims [20]. The most conspicuous element of the accelerator complex, of which an overview is given in figure 4.1, is the LHC ring, which is 27 km in circumference (which, even by the standards of particle accelerators, is quite large) and designed to contain proton (a species of hadron) beams with energies as high as 7 TeV. Where two such beams cross one another, proton collisions with 14 TeV energy may occur. The LHC's beams cross one another at four points around the ring, each one the site of one of the four main experiments.

The LHC is the last step in a series of particle accelerators that brings protons from rest to a final energy of 7 TeV. The series of particle accelerators incorporates two of CERN's previous main accelerators, the Proton Synchrotron and the Super Proton Synchrotron. Throughout, protons are accelerated by applied electric fields, applied within so–called radiofrequency cavities, and contained within the rings by dipole magnets. Magnets with higher pole counts are used to manipulate the profile of the proton beam [21].

Even though the LHC was designed for an energy per beam of 7 TeV, giving a collision energy of 14 TeV, several accidents during commissioning of the machine have necessitated the use of a lower beam energy for the first runs. In 2012, when the

[1] **A** **T**oroidal **L**HC **A**pparatu**s**.

[2] **C**onseil **E**uropéen pour la **R**echerche **N**ucléaire. When the council tasked with creating the european nuclear research laboratory became the organisation tasked with running that laboratory, its name changed to Organisation Européenne pour la Recherche Nucléaire—the European Organisation for Nuclear Research, but the initialism remained. Acronyms, it seems, are not only ubiquitous, but also immutable.

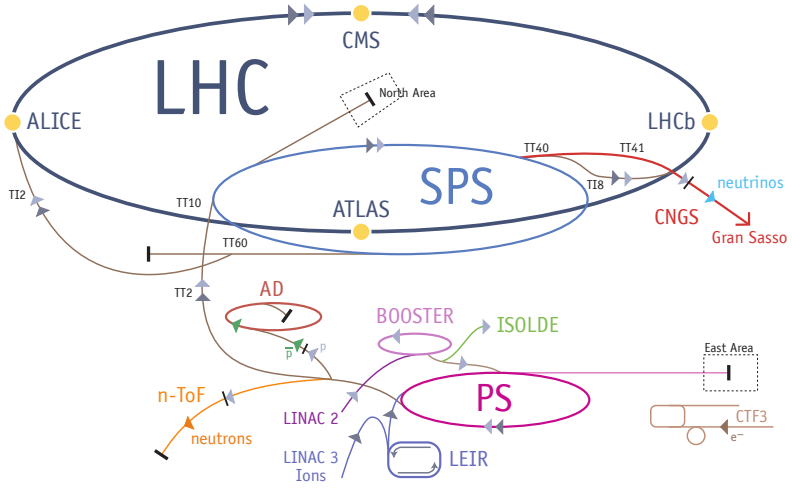

Figure 4.1:
A schematic view of the CERN accelerator complex [19], in which protons or heavy ions used in collision experiments are accelerated through several machines to progressively higher energies. The paths protons can take through the machine are marked with light gray triangles. The dark gray triangles mark the paths taken by heavy ions when the Collider runs proton–lead or lead–lead collision experiments. Protons are 'created' by ionising hydrogen atoms and then injected by LINAC 2 into the Booster ring. From there, protons are accelerated by the Proton Synchrotron (PS) and then the Super Protron Synchrotron (SPS) before finally being sent into the LHC ring. The LHC ring is the largest circular accelerator in the CERN complex, and—at time of writing—in the world, measuring approximately 27 km in circumference.

data that will be used in this thesis was taken, the LHC ran at 4 TeV per beam, for a total collision energy of 8 TeV.

Although we speak of proton beams, protons within the beams are arranged in discrete bunches, occurring at 50 ns intervals. As a consequence, proton collisions occur only within known time intervals, which dictate the timing by which detector readout occurs.

4.2 The ATLAS detector

The ATLAS detector is the largest of the LHC's four detector expermients, and is, as is the CMS[3], a general purpose detector, designed to capture as much information as possible about collision events. To that end, the ATLAS detector is made up of three distinct detector subsystems, layered concentrically about the interaction point, as illustrated in in figure 4.2. From innermost to outermost, these are: the tracking system, the calorimeter system and the muon spectrometer.

ATLAS defines its own coordinate system, centred on the interaction point, where the position in the angular direction, perpendicular to the beam pipe, is measured

[3]The **C**ompact **M**uon **S**olenoid.

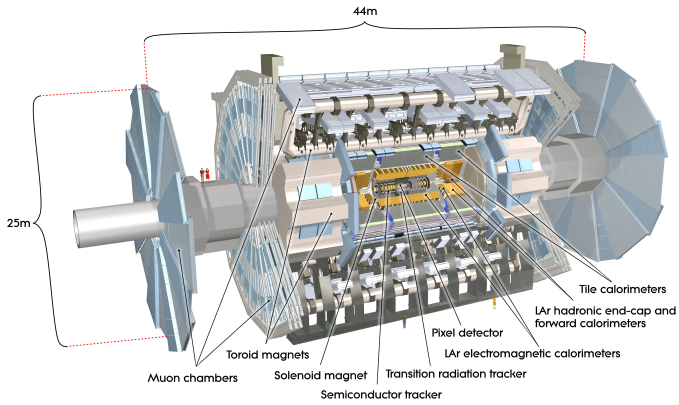

Figure 4.2:
A diagram of the full ATLAS detector [22]. The overall structure is of a layered cylinder centred on the interaction point. We refer to those parts of the detector that make up the wall of the cylinder as the barrel section, and to the ends of the cylinder as the endcap. The electromagnetic calorimeter, which is the detector element that we will make the most use of here, is coloured orange in this drawing.

by the azimuthal coordinate ϕ, and the angle to the beam pipe is measured in pseudorapidity η, which is defined as

$$\eta \equiv -\ln[\tan(\theta/2)] = \frac{1}{2}\ln\frac{|\mathbf{p}| + p_z}{|\mathbf{p}| - p_z}, \tag{4.1}$$

where θ is the polar angle to the beam pipe in radians [11]. The pseudorapidity η is a simple transformation of θ—it is 0 at $\theta = \pi/2$, ∞ at $\theta = 0$ and $-\infty$ at $\theta = \pi$—but is chosen since it is approximately, and for massless particles exactly, equal to rapidity,

$$y \equiv \frac{1}{2}\ln\frac{E + p_z}{E - p_z},$$

which is additive under Lorenz boosts in the z direction [11].

A machine as large and complex as ATLAS would require a large document, such as [23], to describe in comprehensive detail. For the present, a decidedly non-comprehensive description of the three detector layers, in order of increasing relevance to this work, follows.

The muon spectrometer forms the outermost, and most voluminous, part of the detector. As a species, muons, along with neutrinos, are the only types of particles that can regularly penetrate both calorimeters. Capturing neutrinos with ATLAS' mere 7 000 t of material and 270 000 m^3 detector volume [22] is something of a lost cause, however.

The muon spectrometer and the inner detector are both tracking detectors, meaning that they are designed to determine the path of a charged particle that passes through them. By immersing such a detector in a magnetic field, which will deflect a charged particle, the charge sign and momentum of the particle can be deduced from the curvature of the track.

The inner detector is also a tracking detector, which uses two distinct detector technologies to localise the tracks of charged particles that pass through it. In the

innermost layers, detector elements and control circuitry are set on silicon semiconductor wafers. These detect passing charged particles, essentially by allowing the ionisation charge to flip a large transistor, which forms the individual detector element. The outer part of the inner detector, the Transition Radiation Tracker, uses drift straws, long tubes filled with an inert gas, which have a wire, which carries a high voltage charge, suspended along the centre. The ionisation charge left by a passing high–energy particle is attracted to the wire, and read out by detectors attached to its ends as a voltage change. The silicon detector is compact system with a high resolution, whereas the straw detectors can economically cover a large volume.

Both the straw detector and the outer part of the silicon detector—the silicon microstrip detector—have very long detector elements, which can only report that a hit has occurred somewhere along its length[4]. To improve resolution in the long direction of these detectors, successive layers of detector elements are placed at an angle to one another, so that hits on successive detector elements narrow down the possible location of a track. The innermost layer of the silicon detector, the pixel detector, uses a pixel structure rather than a strip structure, and so has adequate resolution in all directions. What is worth noting here is that the tracking detector only directly reports times and—more or less approximate—locations of particle observations. They are only combined into particle tracks during a later analysis step.

There are two calorimeter systems in ATLAS: the (inner) electromagnetic calorimeter and the (outer) hadronic calorimeter. In this context, a calorimeter is a device which attempts to absorb energetic particles in some material, and then measures the amount of energy deposited in the process. All calorimeters in ATLAS are sampling calorimeters, meaning that the absorbing material is divided into layers, with some form of detector inserted between the layers, which sample the flow of energy through the material at various depths. In the barrel section of the hadronic calorimeter—the tile calorimeter, the absorbing material is steel, and the sensitive layers are scintillators, a material that luminesces when exposed to ionising radiation. The light produced there is then guided to photomultipliers for detection.

The remaining calorimeters, which covers both the EM calorimeters and the endcap hadronic calorimeters, are all of a similar design, which has liquid argon as the sensitive material, and are thus called LAr calorimeters. As with the straw detectors, activity in the liquid argon layers are detected by an electrode, which picks up the ionisation left by passing energetic particles. In the barrel LAr calorimeters, the absorbing material is lead encased in thin steel layers. The endcap LAr calorimeters, however, are subjected to much stronger particle fluxes, and so copper, and in some cases tungsten, is used in place of lead, owing to their greater resistance to high temperatures.

4.2.1 The electromagnetic calorimeter

The EM calorimeters are particularly important tools for detecting photons. As such, we devote an entire sub–section to their description.

[4]Some additional resolution can be gained by studying the drift time in the straw detectors.

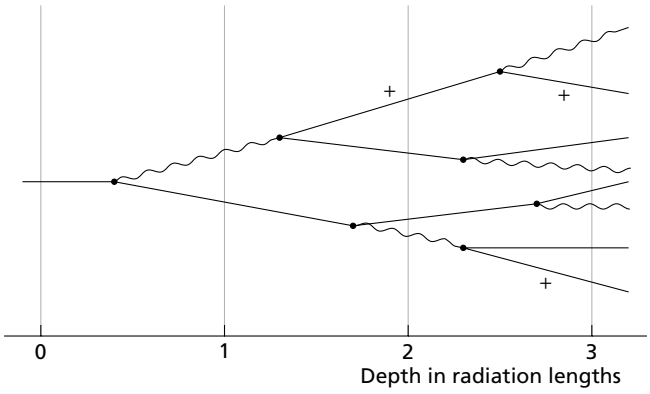

Figure 4.3:
A schematic description of an EM shower developing in an absorbing material, adapted from [24]. Here, a wavy line indicates a photon, a straight line indicates an electron, and a straight line with a '+' a positron. At each split, the two resulting particles carry away half the energy of the original particle. In a sampling calorimeter, a sensitive layer is typically inserted at intervals of one radiation length. ATLAS' LAr calorimeters measure the magnitude of ionisation that is left in the liquid argon by the passage of the particle shower.

In the presence of matter, high–energy photons loose energy primarily through pair production, while electrons loose energy primarily through bremsstrahlung. The typical lengths travelled by both types of particle before undergoing these respective processes—their radiation lengths—depend on the material traversed, but are roughly equal to one another [24]. As illustrated in fig. 4.3, both types of particles will undergo the same sort of evolution as they travel through an absorbing material, splitting into pairs of particles, each with a fraction of the energy of the parent particle, until the daughter particles no longer have sufficient energy to penetrate the absorbing material. Within the calorimeter, this cascade of particles forms a shower structure, an example of which is sketched in fig. 4.4(b). Thus, we can measure the energy of the original particle both by how deep into the absorbing material it penetrates, and by how many daughter particles it produces. In a homogeneous calorimeter, such as the one in CMS, where a single material is used both for absorption and detection, only the amount of activity produced by a hit to the calorimeter is measured. In a sampling calorimeter, where the absorbing material is passive, and activity is sampled by inserting sensitive layers into the absorbing material at intervals, we can measure both the penetration depth, since the thickness of absorbing material in front of the deepest activated sensitive layer is known, and showering activity, by using proportional detectors in the sensitive layers. The radiation length is then a natural scale for the thickness of each layer of absorber. In total, the electromagnetic calorimeter has a thickness of at least 22 radiation lengths.

ATLAS' barrel LAr calorimeters are divided into three layers, which are split into readout bins as illustrated in fig. 4.5. The first layer is very finely divided in the η direction, and its readout cells will on occasion be referred to as 'strips' in the 'strip layer', as opposed to the 'cells' in the other two layers. The detectors function on the same sort of principle as the straw detectors in the inner detector: charged particles leave ionisation trails in the liquid argon, which is picked up on plates suspended in

Figure 4.4:
Several figures, from [22], that illustrate the structure and use of the LAr calorimeters. These are sampling calorimeters, which have an absorbing medium (primarily lead and steel) with layers of detecting medium (liquid argon) inserted regularly to measure particle flux. In ATLAS' LAr calorimeters, rather than having flat layers, the absorbing and sensitive materials are interleaved in an accordion shape, visible in (a) and (b), which allows the detector electronics to be inserted along the gaps between the absorbing plates. Thus, the calorimeters do not need to be interrupted by non–sensitive space for signalling connections.

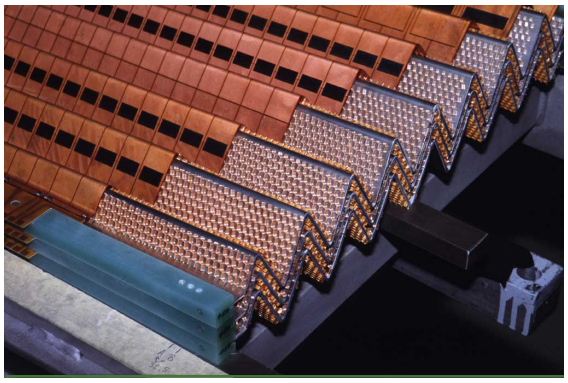

(a) A section of the LAr calorimeter.

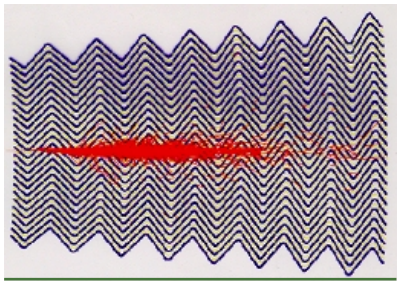

(b) Illustration of a particle shower within the LAr calorimeter.

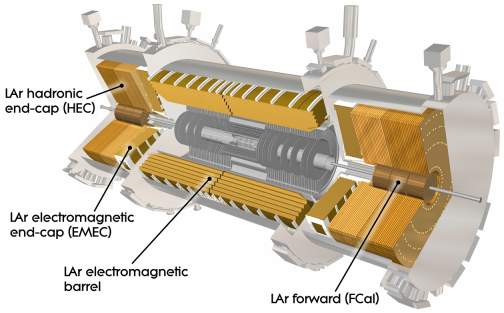

(c) Schematic showing the placement of the LAr calorimeters in ATLAS.

the middle of the LAr gap, which carry a high voltage charge. Each cell functions as a single proportional counter. Thus, the amount of energy deposited in each cell of each layer of the calorimeter is measured by the amount of showering activity in the sensitive layers of that cell.

The absorbing material in the barrel LAr calorimeter are accordion shaped sheets of lead held in steel sheets, visible in fig. 4.4, inserted radially into the detector, so that radiation leaving the detector is still faced with broadly uniform layers of absorbing material, while gaps between them, which hold the detector plates, still run contiguously throughout the depth of the calorimeter. Connections between the detectors in the inner part of the calorimeter and the readout electronics outside the calorimeter can be run through these gaps without needing to create holes in the detectors coverage.

The division of the calorimeter into layers gives us some resolution in depth when attempting to ascertain the shape of a shower. Showers initiated by types of particles

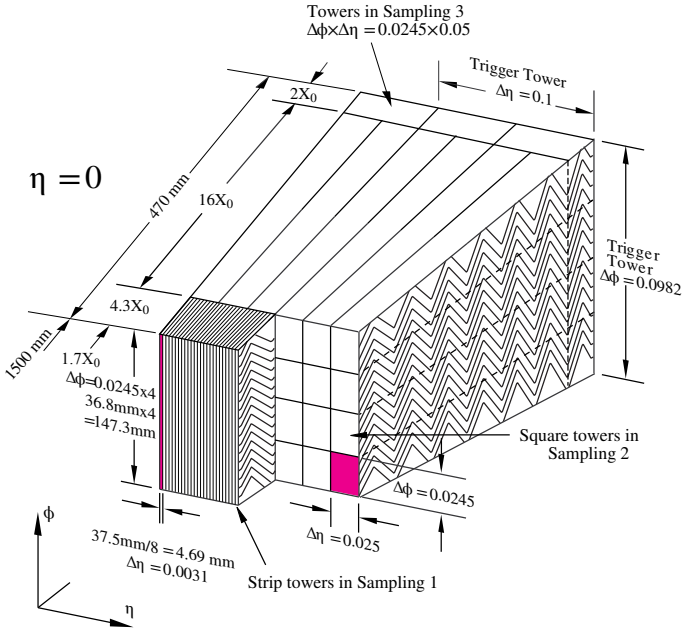

Figure 4.5:
The division of the EM calorimeter into detecting cells [25]. The first layer is divided into thin strips for the greatest resolution in the η direction. The second layer is divided into roughly square cells, and comprises the bulk of the depth of the detector. The last layer is presumed to only be reached by the most energetic particles, and can have a coarser division without loosing resolution. This diagram is of the calorimeter at $\eta = 0$, closest to the interaction point. At higher $|\eta|$, the towers are angled so that they are still pointed toward the interaction point.

other than photons or electrons evolve in a slightly different way, which allows us discern the source of a shower by examining its shape. Additionally, with this shower shape information, we can extrapolate the direction from which a particle entered the calorimeter, which is of particular importance when attempting to trace the origin of unconverted photons, which otherwise leave no trail in the detector.

There is quite a bit of material between the calorimeter and the interaction point, which is not part of the active detector systems, but into which a particle may just as easily deposit energy, in the same way as they do in the absorbing material in the calorimeter. To attempt to correct for this upstream energy loss, the first active layer, called the presampler, sits ahead of the first absorbing layer. Photons that undergo pair production sufficiently deep in the detector for the tracker to resolve at least one of the resulting (anti–)electrons are treated as a separate object type, namely converted photons. Identifying all the detector signatures that may have been left by photons is the first major (relevant) step in analysing the detector's output.

4.2.2 Triggering and readout

While in full operation for the 2012, 8 TeV run, the LHC delivered a bunch crossing in ATLAS' interaction point every 50 ns, or 20 million bunch crossings per second. Reading out the whole detector produces 1.6 MB of information, which, if the detector were read out completely with every crossing, would produce a data rate of 34 TB/s.[5] However, since only a fraction of these crossings will contain interesting physics events, we can reduce the data rate to less prohibitive levels simply by not

[5]For perspective, that is approximately equal to the estimated global IP traffic rate in 2015, according to [26].

recording data from collision that do not produce interesting outcomes. To accomplish this, we need a system that examines events in the detector as they occur, and trigger recording whenever it sees an interesting event. In ATLAS, this trigger system has three levels, which are described in detail in [23].

The level–1 trigger examines detector output in real time. To do so, the trigger logic is run on specialised hardware built in to the detectors themselves. As a result, each trigger only has access to information from the detector its hardware is attached to. Calorimeter triggers, for example, do not have access to information from the tracking system at the first trigger level. Also, computationally intensive tasks, such as track reconstruction, can not be completed in the window of time available to the level–1 trigger, and so are also not available. If a level–1 trigger fires, readouts from every detector element taken during the time window associated with that bunch crossing are passed to the next trigger level, level–2. This trigger is run on the full set of temporarily stored information from an event, on those events which pass the level–1 filter. The final trigger level works with fully reconstructed events and derived physical observables. This requires more time and processing power than is available at the previous levels, but it also identifies interesting events with the same quality of information as will be used in the subsequent analysis. All three triggers in combination cuts the final event rate to 300 events per second, with a peak rate of 600 events.

The rate at which collisions happen within the detector may be summarised in a quantity called the luminosity $\mathscr{L}$. It is defined so that by multiplying the luminosity with the cross section of a process, we get the frequency with which that process occurs in the detector. Integrating the luminosity over time, we get the integrated luminosity, which can be thought of as a measure of how many opportunities for interactions there have been over the period of time being integrated over, independent of the fine details of how the experiment was run.

For this thesis, we shall use data taken during the 8 TeV run in 2012. The amount of data taken at any given time depends on the conditions of the beam, which can be summarised in the instantaneous luminosity, and the conditions of the detector, which may only capture a fraction of the events produced at any given time. Figure 4.6 gives the distribution of integrated and captured luminosity over the course of the year.

Unfortunately, the triggers that are implemented in ATLAS do not guarantee that the readout rate remains within the technical limitations of the readout system. To stay within those limits, a prescale is applied to triggers that select more collision events than it is considered worth keeping,[6] which means simply that a fraction of collisions that pass a trigger are not recorded. The diphoton channel is important to the search for the Higgs boson, however, so, fortunately, no prescales have been applied to the triggers that produce diphotons events.

For this thesis, we will be working with data prepared by ATLAS' e/gamma working group, which has defined the final reconstruction procedures, as well as final requirements on data quality and detector status. After these requirements are applied, the 20.3 fb^{-1} of data generated by the ATLAS detector is reduced to 18.301 fb^{-1}, avail-

[6] Explaining how worth is assigned to event types is not a topic within the scope of this thesis.

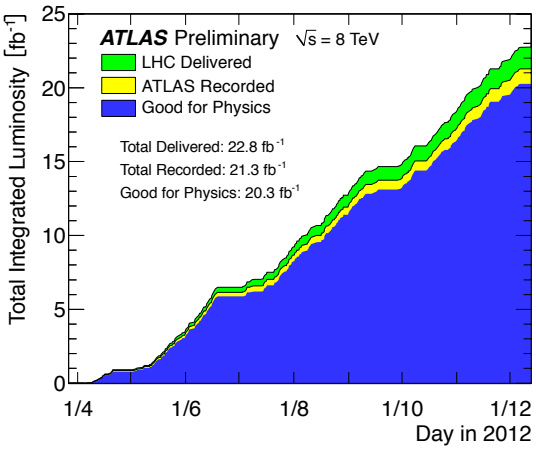

Figure 4.6:
A plot [27] showing the integrated luminosity delivered by the LHC (green), recorded by ATLAS (yellow), and fulfilling data quality criteria (blue), over the course of the 8 TeV run in 2012.

able in the `NTUP_PHOTON` format. Full (non–public) information at [28], or public in [29].

4.2.3 Photon identification

In broad terms, we may view information coming from the detector in terms of energy clusters in the calorimeters or tracks in the inner detector. Assigning calorimeter deposits to discrete clusters is a task that can be approached a number of ways, both subtle and complex, however at the low–level trigger stage, the straightforward sliding window method is used [30]. A rectangle of fixed size is defined by combining calorimeter cells, and the energy within is summed. This 'window' is then 'slid' across the entire calorimeter, and a cluster candidate is proclaimed whenever the energy within the window reaches a local maximum above a predefined threshold value.

Assuming that every charged particle leaves both a track in the inner detector and a cluster in the calorimeter, we interpret every cluster in the calorimeter that can not be associated with a track as the signature of a neutral particle. Each of these neutral particles might be an unconverted photon, and so every cluster without an associated track is added to the list of photon candidates.

As previously mentioned, converted photons are photons that undergo pair production "in flight." As such, we expect the detector signature of such events to be a positively and a negatively charged track with a common vertex away from the interaction point. Any set of measurements that match this signature may be added to the sequence straight away, however since track reconstruction is an imperfect process, especially in the straw detector, we include also any electron candidate, whose track is reconstructed solely from hits in the straw detector.

These steps form a selection algorithm, which creates a list of photon candidates for every bunch crossing in ATLAS [29].

This list will of course also contain many non–photons: π^0 mesons also create calorimeter hits with no associated track, and QCD jets can mimic converted photons, among other possibilities. To attempt to sort genuine photon events from impostor

events, we study the shape of the shower left in the calorimeter. To that end, we define the following shower shape variables:

- R_{had}, the ratio of energy deposited in the hadronic calorimeter to the cluster energy in the EM calorimeter. Hadronic showers are expected to penetrate deeper into the hadronic calorimeter than EM showers.
- In the middle EM calorimeter layer, non-EM showers spread wider than electromagnetic ones. The variables that measure the shape of the shower in this layer are:
  - R_η, the ratio in η of cell energies in 3×7 versus 7×7 cells.
  - R_ϕ, the ratio in ϕ of cell energies in 3×7 versus 7×7 cells.
  - $w_{\eta 2}$, the width of the shower in the η direction.
- The strip layer, with its greater resolution in η, can pick out some of the internal structure of a jet. Hadron showers tend to show more than one maximum. Variables that measure the shape in the strip layer are:
  - w_{s3}, the shower width for three strips around the maximum strip.
  - $w_{s\,\text{tot}}$, the total lateral shower width in the strip layer.
  - F_{side}, the faction of energy deposited outside a core of 3 central strips, but within 7 strips.
  - ΔE, the difference in energy of the strip with the second largest energy deposited and the strip with the smallest energy deposited between the two leading strips.
  - E_{ratio}, the ratio of the energy difference associated with the largest and second largest energy deposits, over the sum of these energies.

Converted and unconverted photons will of course have different signatures in these variables. Thus, the photon identification algorithm also includes a step which calibrates and corrects the detector response to these two object categories [29].

Cuts made in these variables form the selection criteria that are used to divide the sample of photon candidates into those that are to be considered actual or impostor photons. The full list of variables above forms the tight selection criteria, while a shorter list, consisting of R_{had}, R_η and $w_{\eta 2}$ form the loose selection criteria. Separate cut values in these variables exist for different η ranges. A complete description is available in [31].

4.3 Detector simulation

In chapter 3, we employed Monte Carlo techniques to simulate the outcome of the processes we wish to study. From this procedure, we retain perfect knowledge of every

step in the evolution of those events. This is very unlike the picture that the detector will give us of the events in the actual, physical experiment.

The actual events will be viewed through the 'lens' of the ATLAS detector. The detector only registers changes in voltage in its individual detector elements. The objects that analyses such as this will deal with—tracks, energy clusters and jets—are reconstructed from the raw reading in individual detector elements by computer algorithms. Additionally, the final state particles produced by the hard process, as simulated by pythia, could potentially interact with the material that makes up the detector and decay, split or convert before or during their detection, while the detector does not fully or accurately detect all the particles that pass through it. Because of this, it is necessary to also simulate how the detector interacts with the final state particles we generated in the previous section, to properly relate that information with experimental data.

Furthermore, as discussed above, the collisions that the LHC produces are not between single protons, but between bunches containing of the order 10^{11} protons [19], which follow one another at 50 ns intervals. Because of this, particles produced by more than one proton collision will be present within the ATLAS detector during the recording window for each bunch crossing, either from multiple protons in the current bunches interacting, or from the products of the previous or subsequent bunches intruding into the recording window. For the period in question, the average number of interactions per crossing easily exceeds 20 [27]. Collectively, we refer to these—for our purposes—extraneous events as pileup. The solution for reproducing the effects of pileup in simulated events is to randomly pick an appropriate number of generic pileup events from a dedicated set of simulated events, and add them on top of the interesting event, to approximate the complete product of a collision in the detector. Since the distribution of numbers of interaction to be added per event were specified before the 8 TeV run was completed, the expected distribution does not match the measured one exactly. To account for the difference, Monte Carlo events are reweighted by their number of interactions to correct for this deviation [32].

Since these steps must be followed every time a Monte Carlo set that approximates the ATLAS experiment is produced, the information and computer programs needed to run them are provided in a standard package by the ATLAS Collaboration. The simulation of the interaction between particles and the physical detector comes in the form of a geometry model for GEANT4 [33], a program that can simulate the interaction between high–energy particles and matter.

The real detector has a finite energy resolution, which is not reflected in the Monte Carlo events, for which we have an exact momentum. To overcome this, we smear the energies given by the simulation—that is shift the energies by a random amount chosen from a gaussian distribution with a width chosen to reflect the resolution of the detector [34].

The effect that the detector simulation has on the invariant mass distribution of the event samples created above is shown in figure 4.7.

Unlike the effects of parton level processes and hadronisation applied to the Monte Carlo samples previously, which could be represented by a simple shift in magnitude,

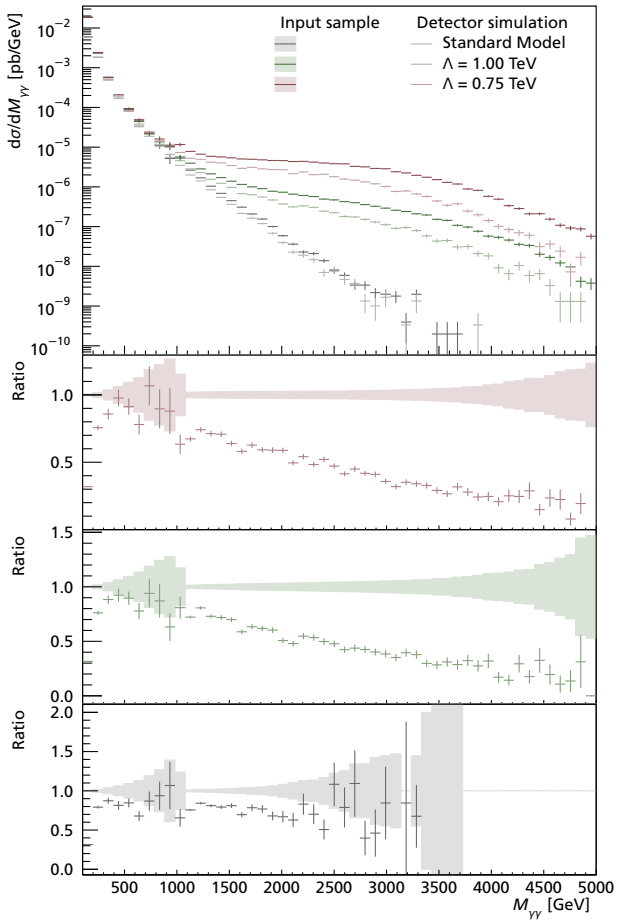

Figure 4.7:
A plot comparing the event samples produced by CalcHEP and pythia with the results of running those event through the detector simulation available through GEANT4. We note a clear trend toward fewer reconstructed photon pairs at higher invariant masses. Since the new term being studied alters the abundance of photon pair with high invariant masses, this effect would impact the final result of this analysis if not included.

these plots demonstrate a non–trivial behaviour, which correlates with $M_{\gamma\gamma}$.

Once the simulation of detector response to a simulated event is done, it can be cast into the same format as the output from the detector system, containing the same variables describing the same types of objects. This set of pseudo-experiments, once normalised to the luminosity of the 8 TeV run, should be directly comparable to the experimental data.

5 Data preparation

For the present analysis, we will use events that passed the `2g40_loose` level–1 trigger, which requires that the EM calorimeter reports two energetic regions with at least 40 GeV of transverse energy that pass the loose selection criteria, described previously in chapter 4.

The datasets have been retrieved in the `NTUP_PHOTON` format, which is streamlined to contain information relevant to photon analyses, and easily readable by ROOT. The dataset used contains events corresponding to 18.301 fb^{-1} of integrated luminosity.

On each of the prospective photons in this dataset, we impose a series of selection criteria:

- **otx and phoClean cut:** Object quality cuts, which cut out events too close to non-functioning or noisy detector elements, and events taken while the detector was in a non-optimal state.
- **ID cut:** Objects that did not pass photon identification, or do not satisfy the loose selection criteria after reconstruction, are eliminated.
- **kinematics cut:** Ensures that objects do not have $|\eta|$ greater than 2.37, which is the forward limit of the first layer of the EM calorimeter, or in the range between 1.37 and 1.52, which is the transition region between the barrel and endcap calorimeters. Also ensures E_T greater than 50 GeV, which clears the turn–on curve[1] of the `2g40_loose` trigger.
- **N_events cut:** Ensures that each event has at least two photons that pass the above criteria.
- **PV cut:** Ensures that a photon pair can be associated with a primary vertex—that is, there must be at least one primary vertex within 3σ of the reconstructed z coordinate of the common vertex of the photon pair—which, additionally, must have at least 3 tracks associated with it, and be within 3σ of the beam spot in the x and y coordinates.

[1] Since the trigger cuts on a hardware value which is correlated with, but not identical to, the reconstructed E_T, the reconstructed E_T value of the lowest events that pass the trigger fall in a distribution around the trigger value. The rising curve at the beginning of the distribution is the turn–on curve.

- **selected photons cut:** Rejects diphoton candidates where one or both participants were not selected in the previous cuts.

If more than one photon pair are selected in a single event, the pair with the highest p_T leading photon is selected.

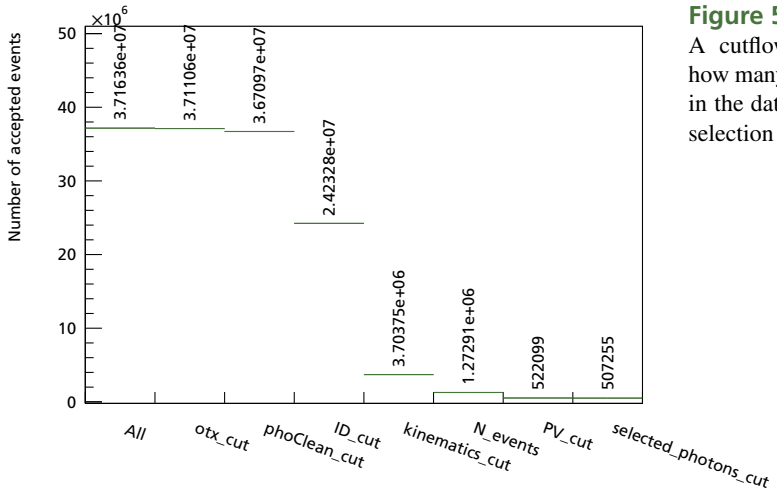

Figure 5.1:
A cutflow diagram, showing how many photon pairs remain in the dataset after each of the selection criteria are imposed.

The number of photon pairs remaining at each step of the cut procedure is plotted in figure 5.1

What remains after these cuts have been applied is a purer sample of photons than we had before, however the sample will still contain a background of events that do not come from the processes that we wish to study. An estimate of this background is required.

5.1 Data driven background estimation

The background that remains in the signal sample after these criteria have been applied can be estimated in a number of ways. Here, we shall attempt to quantify the magnitude of the background by examining the data. Background, in this context, means events where one or both photons were some other type of object misidentified by the detector as a photon. This might include electrons whose track was not properly reconstructed, jets or other neutral particles, such as the π^0. The ABCD method attempts to remove events that have a signature different from the signal in two selected variables.

5.1.1 The ABCD method

We assume that it is possible to extrapolate the shape of the distribution of background events that pollute the signal sample from the distribution of events that occur well

away from the signal region. The ABCD method assumes that the distribution of background events has the same shape in the signal region as it does in a control region. There will still be a scale difference between the two, which can be determined by examining a different control region.

This is also known as the two–dimensional sideband method [36]. The following description may be aided by the illustration in figure 5.2.

To reiterate, we need to examine our sample of signal and background data points in terms of two uncorrelated discriminating variables, call them x and y. With this, we can split the data set into four regions:

A: The signal region in both discriminating variables. This region should contain all signal events.

B: The signal region in the y variable, but not in x. We assume that the distribution of background events in y in this regions will have the same shape as the distribution of background events in y in the signal region, A.

C: As above, but with x and y exchanged.

D: The control region for both variables. Once again, we assume that the distribution of background events has the same shape for either variable in the control region as it has in its signal region. We expect the distribution in x to have the same shape in the D region as it does in the B region, for example.

Thus, the distribution in x of background events in the A region, A_{bck}, is assumed to be the shape of the distribution of events in the C region, scaled so that the distribution of events in x in the B and D regions have the same magnitude:

$$A_{bck} = C\frac{B}{D}. \tag{5.1}$$

The signal distribution must then be given as

$$A_{sig} = A - A_{bck}. \tag{5.2}$$

As we are working with events with two photons, both of which give rise to independent backgrounds, this procedure must be repeated for the subleading photons as well. For the subleading photon candidate, we look at the sample of photon candidates that are the subleading partner of a selected photon in the signal, A, region of the distribution of leading photon candidates. Carrying out the ABCD procedure on the sample of subleading photons gives us Aa_{bck}, an estimate of the number of selected photon pairs where the leading photon is in the A region and the subleading photon is a part of the background in the Aa region. Using (5.2), we can now write the number of events in the signal–signal region as

$$\begin{aligned} A_{sig}a_{sig} &= (A - A_{bck})a - (A - A_{bck})a_{bck} \\ &= Aa - A_{bck}a - Aa_{bck} + A_{bck}a_{bck} \\ &= Aa - [Aa]_{bck}. \end{aligned} \tag{5.3}$$

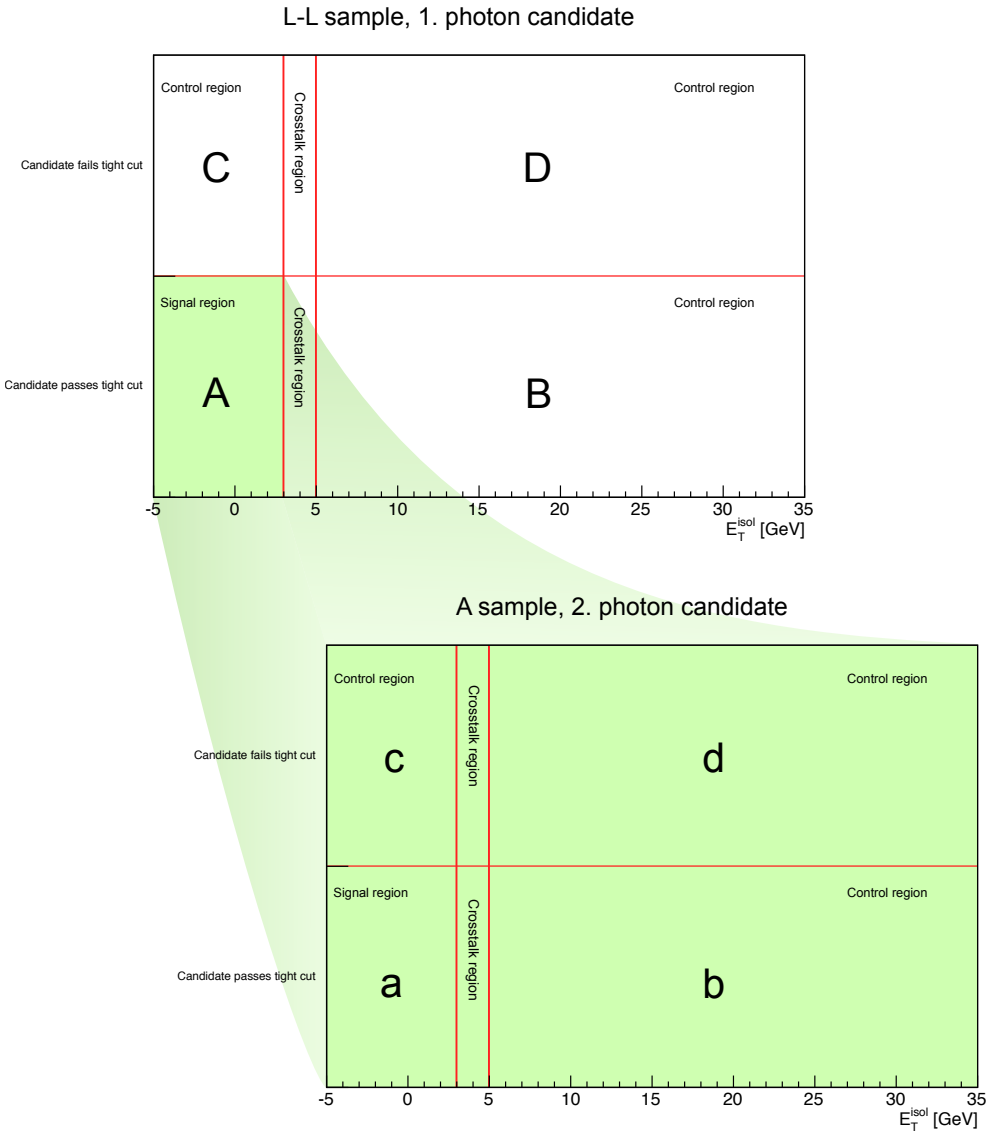

Figure 5.2:
Illustrating the two–step ABCD method, adapted from [35] using the 'tight' selection criteria and the isolation energy: the full set of diphotons (the L-L sample) is split into four groups—A, B, C and D—according to the discriminating variables for the leading photon. Signal photons are now confined to the A region. The events in the C region can be used to estimate the shape, and the B and D region can be used to estimate the magnitude of the distribution of background events in the signal region. The procedure is then repeated for the subleading partner photons of the events in the A region. This gives an estimate of the distribution of background events in the combined signal (Aa) region.

Aa is the number of events in the Aa region, which is readily available. Of the terms that contribute to the total background $[Aa]_{bkc}$, Aa_{bck}, the total number of background subleading photons in the Aa region, is determined by taking

$$Aa_{bck} = Ac\frac{Ab}{Ad}, \tag{5.4}$$

analogous to how A_{bck} sample was found in eq. (5.1). We find $A_{bck}A$, the total number background leading photons in the Aa region, and $A_{bck}a_{bck}$, the number of photon pairs in the Aa region where both members are background photons, by multiplying Aa and Aa_{bck} by

$$f_{bck} = \frac{A_{bck}}{A}, \tag{5.5}$$

the fraction of background events in the leading photon A sample. Thus, the total estimated background in the AA region is given by

$$[Aa]_{bck} = \frac{A_{bck}}{A}(Aa) + Aa_{bck} - \frac{A_{bck}}{A}(Aa_{bck}), \tag{5.6}$$

which we can interpret as the number of data points where the leading photon was a background plus the number of data points where the subleading photon was a background, subtracted the number of data points where both photons were background events, which would have been double counted.

For the diphoton sample, the choice of the two discriminants are the 'tight' selection criteria, which were described in chapter 4, and the transverse isolation energy, E_T^{isol}, the energy deposited in the calorimeter in a cone with radius $R \leq 0.4$, but outside $R \leq 0.2$, where

$$R = \sqrt{\Delta\phi^2 + \Delta\theta^2}.$$

The signal region is defined as $E_T^{\text{isol}} \leq 3$ GeV. Allowing a crosstalk region of 2 GeV, which means the background region is 5 GeV $\leq E_T^{\text{isol}} \leq 25$ GeV, produces the distribution of E_T^{isol} for leading photons and subleading photons in the 'A' sample is given in figure 5.3. As the figure shows, the tight and loose selections are identical in the background region, whereas they diverge in the crosstalk region, which is the desired behaviour.

Performing this process for each bin in $M_{\gamma\gamma}$, we obtain the distribution of background events shown in figure 5.4. Note, though, that the plots of E_T^{isol} in fig. 5.3 shows the distribution for all $M_{\gamma\gamma}$ bins combined.

5.2 Comparison to SM MC

The ATLAS Collaboration has produced a large selection of Monte Carlo data sets from which we choose a selection to represent a Standard Model prediction. These sets, like those that were created in chapter 3, have been through a detector simulation step, so that detector response has been taken into account, and they are in the same format, and contain the same types of information, as the data sets produced by the ATLAS

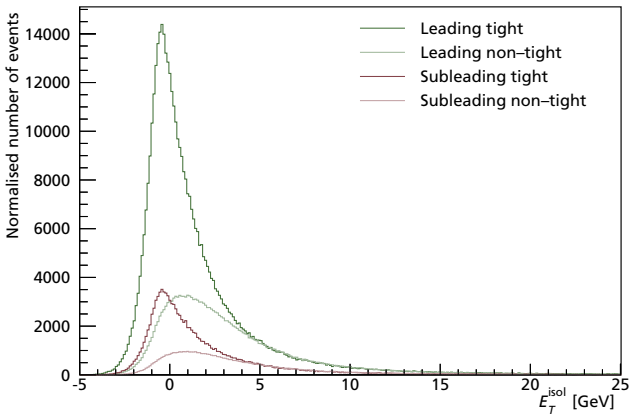

Figure 5.3:
The transverse isolation energy E_T^{isol} for the tight and non–tight photon selection of the leading photons, and for the set of subleading photons with partners in the 'A' sample. The non–tight samples have been scaled so that the D region contains the same number of events as the B region. For both sets of samples, the shapes of the distributions overlap after the scaling, which supports the assumption that the shape of the background distribution is the same in the signal region as well.

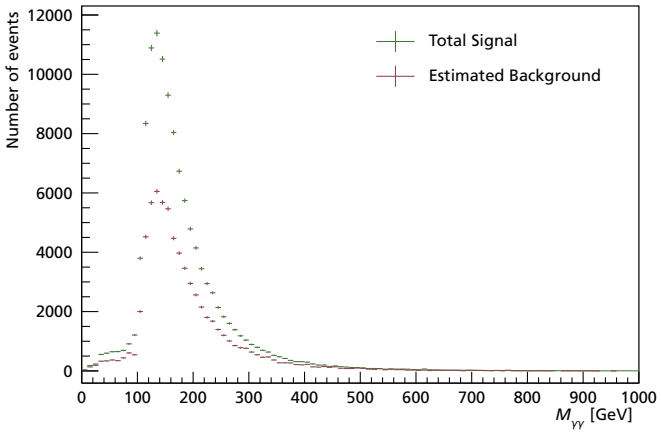

Figure 5.4:
The distribution of background events in $M_{\gamma\gamma}$ estimated from data with the ABCD method, along with the distribution of diphoton events given by the data.

detector. Thus, these sets can be subjected to the same event selection machinery as was developed for as the data above.

The set we choose to represent $qq \to \gamma\gamma$ signal[2] would ideally be precisely comparable to the SM prediction we produced with CalcHEP in chapter 3, however no such set turns out to be available. The set that is available includes several processes that produce γjet final states, which for our purposes are considered a background process. In order to directly compare the ATLAS $\gamma\gamma$ set with the CalcHEP set, we implement, in addition to the event selection already defined, a filter to sort out, event by event, all those events that did not produce two photons in their hard process.

To represent the background to the process under study, we examine a number of MC sets[3] for significant contributions that pass our selection criteria. Among these, the two which provide the most significant contribution within the signal region de-

[2]See appendix A.1
[3]See appendix A.5

scribe events with γjet final states, and events that feature a $Z \to ee$[4] decay. These processes might produce false positives either by emitting hard photons through bremsstrahlung or by false identification of electrons as converted photons. The invariant mass distributions are plotted in figure 5.5, along with the signal and estimated background distributions found above, and the distribution of events found in the ATLAS $qq \to \gamma\gamma$ MC set, after selection criteria have been applied.

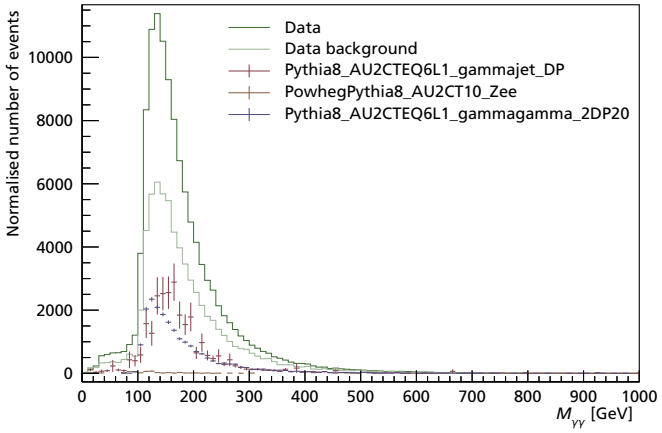

Figure 5.5:
The distribution of invariant masses of events that pass the selection criteria, found in ATLAS MC sets that describe the SM signal process, and selected processes that might contribute to the background. These are compared with the distribution of events found in data, and their estimated background.

Here, the γjet MC set has been composited from five different MC sets with successively higher minimum cuts on p_T[5]. We combine them by picking those events from a given set in which both selected photons have reconstructed p_T greater than 1.15 times the initial low cut for the set, and less than 1.15 times the initial low cut for the next set. We choose a cut above the initial value to be clear of any effects of the cut.

Dataset name	Measured/expected events	
Data	115915	
Estimated background	67640	$\pm$ 260
Pythia8_AU2CTEQ6L1_gammajet_DP	26700	$\pm$1610
PowhegPythia8_AU2CT10_Zee	472	$\pm$ 50
Pythia8_AU2CTEQ6L1_gammagamma_2DP20	20480	$\pm$ 210

Table 5.1:
Table listing the number of measured or predicted event in each of the data sets included in the analysis.

We note in figure 5.5 and in table 5.1 that the relative contribution from the $Z \to ee$ process is essentially negligible. It contains no events at all that pass the selection criteria, with an invariant mass above 300 GeV, which is well below where we expect to see an effect from the contact interaction. Thus, we will neglect this contribution going forward.

[4] See appendix A.4
[5] See appendix A.3

It is our assertion, then, that the observed distribution in data is reproduced by the ATLAS Monte Carlo data sets with $\gamma\gamma$ and γjet final states. To test this assertion, we combine these data sets, and process them in the same way as we did to the data sample above. That is, we use the ABCD method to estimate the proportion of events in this data set that are identified as background events. We may then compare the MC signal distribution (mc) with the signal distribution found in data by subtracting from it the background distribution estimated in Monte Carlo (mc_{ABCD}) and adding in stead the background distribution estimated in data ($data_{ABCD}$):

$$mc_{\text{comb}} = mc - mc_{ABCD} + data_{ABCD}$$

Figure 5.6 shows the result.

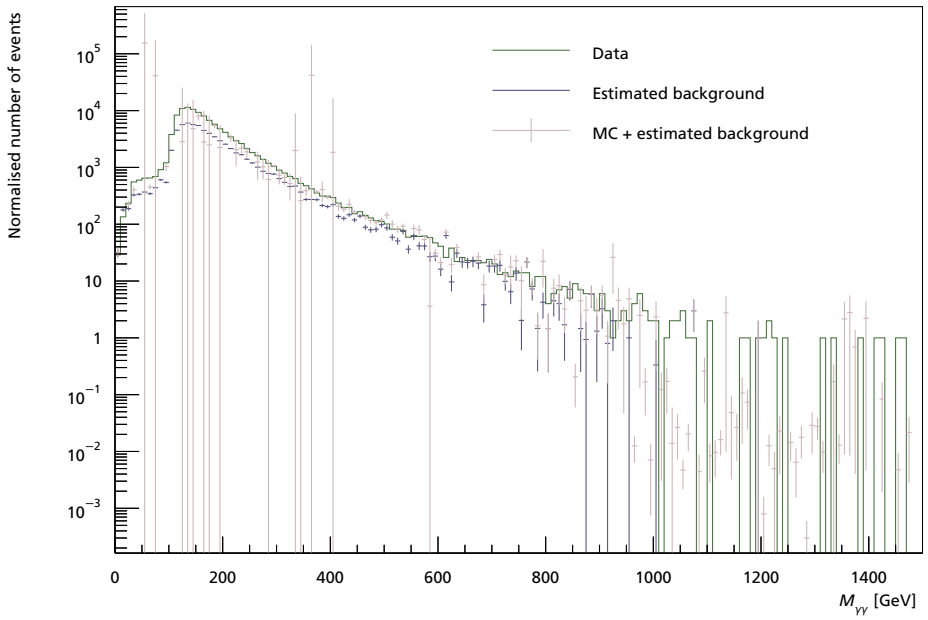

Figure 5.6:
The distribution of invariant masses produced by combining the ATLAS MC sets that best describe the signal processes, from which is subtracted the background contribution found by applying the ABCD method to this set, and to which is added the background contribution estimated in data above.

The plots in this figure have several features worth remarking upon. First, as should also be visible in fig. 5.5, the MC sets for the γjet processes have relatively poor statistics, which leads to high event weights and thus large errors, especially in the invariant mass range below 200 GeV. This is exacerbated by the ABCD method, which results in the very large errors in some bins. The use of the ABCD method to subtract a background–like part of the distribution of MC events has also resulted in some bins of this distribution having negative content, which is why the combined distribution drops below the estimated background in a few bins around the peak. Second, both the distribution of background events estimated in data and the $\gamma\gamma$ MC set have almost no events with invariant mass larger than 1 000 GeV, which is the

reason for the sharp drop at around that value. Unlike the first issue, this lack of statistics affects the most important part of the invariant mass range for estimating Λ, and so we will be forced to attempt to extrapolate the shape of the distribution in this region.

With these caveats, however, the distribution of Monte Carlo events matches the distribution of events in data quite well.

6 Analysis

Recalling from chapter 2 that we may express the number of predicted events in a given bin in the $M_{\gamma\gamma}$ as a second order polynomial in Λ^{-4} with coefficients a, b and c, our aim here will be, first, to determine, for each bin, the coefficients of this polynomial. Second, using a maximum likelihood fit, to determine a most likely value of Λ, and a confidence interval on that value.

6.1 Corrections to Monte Carlo samples

In chapters 3 and 4, we produced, among others, a sample of Monte Carlo events that gives the SM prediction for the distribution of events. Since we discovered above, that the ATLAS $\gamma\gamma$ Monte Carlo sample gives a distribution of events that matches data well, we will compare these two samples to asses how well our SM prediction matches data. In doing so, we encounter a few problems.

First, it appears that the procedure which should correct for pileup in the detector simulation procedure has not functioned as intended. During detector simulation, the events produced for this thesis are assigned only a very limited range of values for the number of interactions per bunch crossing. Ordinarily, the pileup correction procedure expects a distribution of events per bunch crossing that covers the same range as found in data, and simply reweights each event, so that the shape of the distribution in MC is altered to resemble the one found in data. Since the distribution of numbers of interaction per bunch crossing available, the distribution found in data can not be recovered in MC.

Since this appears to be a technical glitch, we will substitute a reweighting in the number of reconstructed primary vertices—vertices considered to originate directly from interactions between protons—in each event. The distribution of numbers of primary vertices in the present MC data set is compared to the one found in the ATLAS MC set in figure 6.1.

The second issue we encounter is in the distribution of E_T^{iso}, which is much broader in the CalcHEP MC set than in the ATLAS one, as illustrated in figure 6.2(a). Assuming that the distribution in the CalcHEP sample is just the one in the ATLAS sample, but broadened and shifted slightly, we develop a mapping function to reverse that effect:

$$E_{T,\text{mapped}}^{\text{iso}} = \frac{E_T^{\text{iso}}}{4.574} - 0.020 \text{ [GeV]}. \tag{6.1}$$

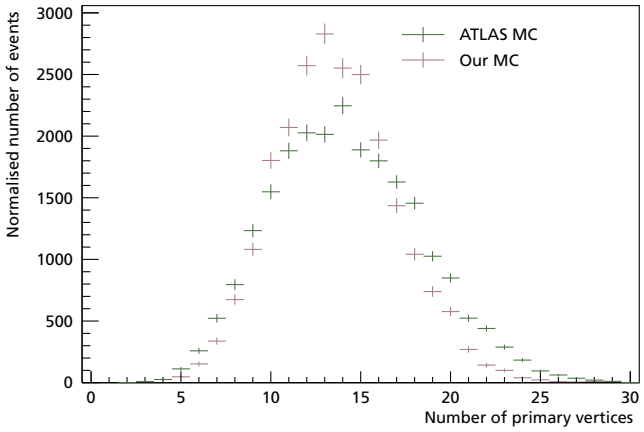

Figure 6.1:
The distribution of the number of reconstructed primary vertices in the ATLAS $\gamma\gamma$ MC set and in the CalcHEP MC set produced for this thesis, normalised to the same number of events.

The result of applying this function is shown in fig. 6.2(b).

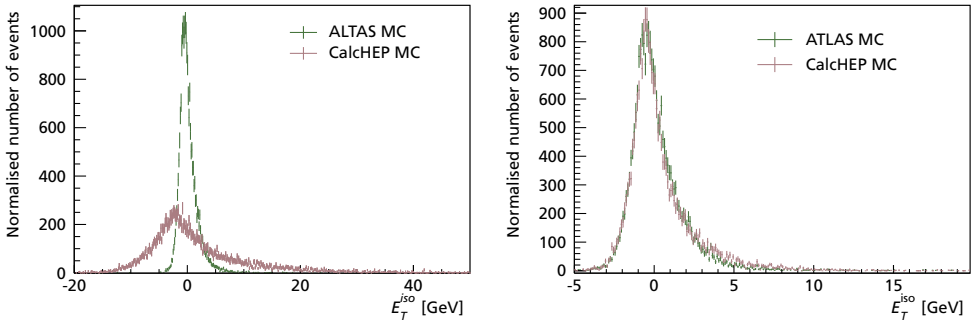

(a) Before application of mapping function.

(b) After application of mapping function.

Figure 6.2:
The distribution of E_T^{iso} in the ATLAS MC set compared with the distribution in the CalcHEP MC set. In (b), a mapping function which applies a scale and offset to the values for the CalcHEP MC has been applied.

These distributions are now very close to being identical. We correct the remaining discrepancy by reweighting the CalcHEP sample.

The weights found above are assigned to the Monte Carlo samples on an event–by–event basis. These weights will of course carry an uncertainty, which can be derived by simple error propagation from the uncertainties of the histograms used to define them. As these weights are assigned event–by–event, we can track the magnitude of uncertainty assigned to each bin of $M_{\gamma\gamma}$ by taking the root square sum of the errors on the weights of each event placed in that bin. This error must then be included in the systematic uncertainties on the analysis.

Finally, the CalcHEP sample only included events produced by the tree level process, whereas the ATLAS sample also includes the contribution from the box diagram shown in fig. 2.8. So, to meaningfully compare the two, we must know the contribu-

tion from the box diagram. This, we glean from another ATLAS MC sample[1], which provides a $M_{\gamma\gamma}$ distribution illustrated in fig. 6.3. As with the estimated background, this distribution has insufficient statistics to accurately represent the shape of the distribution in the interesting region above 1 000 GeV, forcing us to extrapolate the shape of this distribution as well.

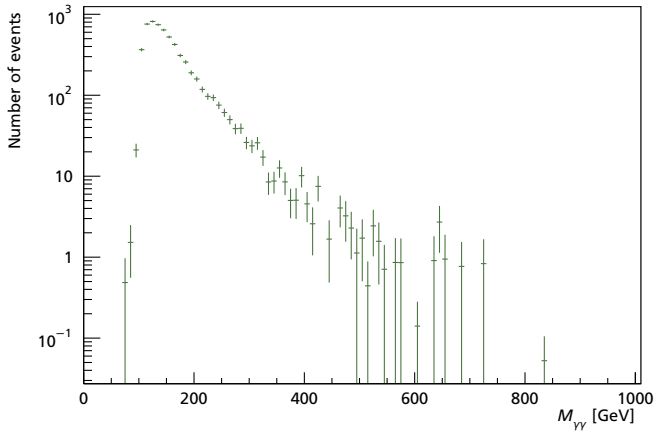

Figure 6.3:
The distribution of invariant masses in the ATLAS box diagram data set.

Adding this to the CalcHEP sample, we get the distribution in fig. 6.4. As should be evident, there is still a deficit in the CalcHEP sample. The box diagram contribution added to the CalcHEP sample was produced by a different generator than was used to generate the ATLAS $\gamma\gamma$ sample, which was not necessarily configured with the same parameters as was used for the present sample, or the ATLAS sample could contain effects from interference between the diagrams which simply adding together samples does not capture. In any case, to be comparable to data, both MC sets must be combined with the γjet sample. The two combined samples will be consistent within their errors.

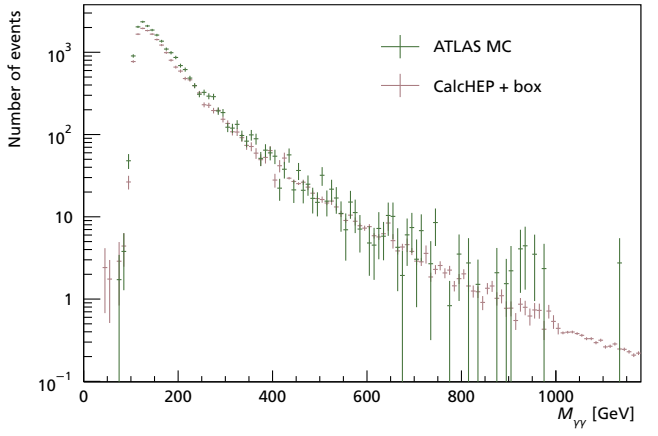

Figure 6.4:
Comparing the ATLAS distribution with the one produced by CalcHEP, combined with a distribution for the box diagram contribution.

[1] See appendix A.2

As the estimated data background (see fig. 5.6) and box diagram (see fig. 6.3) distributions have the same sort of shape, it is natural to combine them before attempting to extrapolate a shape. The function we fit to this distribution has the expression, suggested by [37]

$$f(x) = \underline{7.9\,10^{-5}} \left(\frac{1-x}{8000}\right)^{\underline{22.5506}} \left(\frac{x}{8000}\right)^{-\left[\underline{7.203553}\ \underline{-0.631809}\ln\frac{x}{8000}\right]}, \qquad (6.2)$$

where the four underscored numbers are the fitted parameters. x has been scaled by $8\,000^{-1}$ GeV^{-1} in an attempt to achieve parameter values close to 1. The function is plotted along with the histogram it was fitted to in figure 6.5. This fit, and all further fits, were carried out using ROOTs fitting procedures [38].

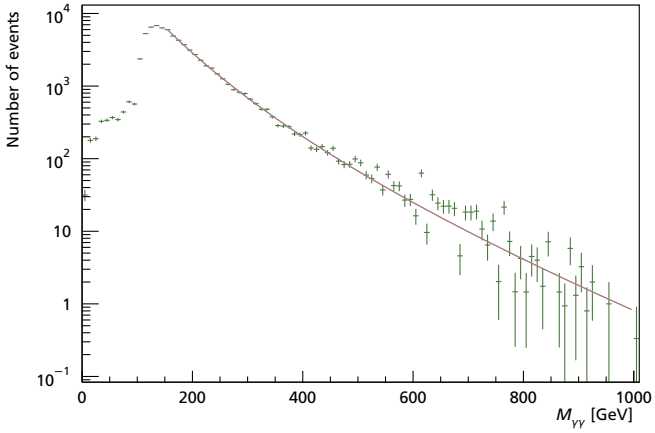

Figure 6.5: Extrapolating the truncated backgrounds by fitting a function. The fit has χ^2 / ndf = 237.2 / 74.

6.2 The polynomial coefficients

Now satisfied with our Monte Carlo samples, we turn toward extracting the coefficients to the polynomials that will allow us to vary Λ. As is evident from the plots of the distributions in figure 6.6, the number of expected events in each bin is subject to relatively large statistical fluctuations. Since the coefficients for each polynomial is determined solely from these three points, the resulting quadratic function may look drastically different from bin to bin. One approach to reducing the statistical fluctuations is to simply combine sets of adjacent bins, rebinning, or to apply some form of smoothing procedure. Here, however, we will attempt to fit a function to each distribution. In addition to smoothing out fluctuations between bins, fitting functions allows us to incorporate some additional knowledge about the relationship between these distributions into our extrapolation of their shape.

Since we have assumed constructive interference between the new interaction and the Standard Model, we know that a distribution which has a contribution from the new interaction, at any strength, must have a number of expected events at least equal to the number of events expected in the Standard Model case at any point. Also, the

Standard Model contributes equally in each distribution, thus the shape of each distribution must be the shape of the Standard Model contribution plus an additional contribution. We select for the shape of the Standard Model distribution the function

$$f_{SM}(x) = p_1 \left(\frac{1-x}{8000}\right)^{p_2} \left(\frac{x}{8000}\right)^{-\left[p_3 + p_4 \ln \frac{x}{8000}\right]}, \tag{6.3}$$

the parameters of which must be shared among all three functions. This is the same type of expression as was used to fit the shape of the background distribution in the previous section. The additional contribution from the contact interaction does not follow this shape of distribution. To describe the shape of the additional contribution, we select, among all possible functional dependencies, an expression with a small number of parameters, which once fitted to the distribution, describes the shape well, with a good χ^2.

We describe the shape of the contribution from the new interaction with functions of the form

$$f_{\Lambda=1.00/0.75}(x) = f_{SM}(x) + p_{5/10} \exp\left[-\frac{1}{2}\left(\frac{x - p_{6/11}}{p_{7/12}}\right)^2\right] + \exp\left[p_{8/13}\frac{x}{8000} - p_{9/14}\right], \tag{6.4}$$

where we have attempted to indicate the parameter numbers belonging to the function describing the contribution at $\Lambda = 1.00$ TeV resp. 0.75 TeV with two indexes separated by a slash. This is effectively a Gaussian plus an exponential. We fit the distributions in the range above 150 GeV, which clears the effects of the minimum p_T cuts, and below 3 000 GeV, where the SM sample runs out of statistics.

The results of fitting these functions simultaneously is shown in figure 6.6.

The fit estimates the parameters to be, for the SM curve:

$$\begin{aligned} p_1 &= 7.81 \times 10^{-6} \pm 0.31 \times 10^{-6} \\ p_2 &= 6.96 \pm 0.14 \\ p_3 &= 6.894 \pm 0.018 \\ p_4 &= -0.553 \pm 0.003 \end{aligned}$$

For the $\Lambda = 1.00$ TeV curve:

$$\begin{aligned} p_5 &= 0.014 \pm 0.002 \\ p_6 &= 2540 \pm 61 \\ p_7 &= 476 \pm 96 \\ p_8 &= -11.6 \pm 0.6 \\ p_9 &= 0.12 \pm 0.09 \end{aligned}$$

And for the $\Lambda = 0.75$ TeV curve:

$$p_{10} = 0.19 \pm 0.03$$

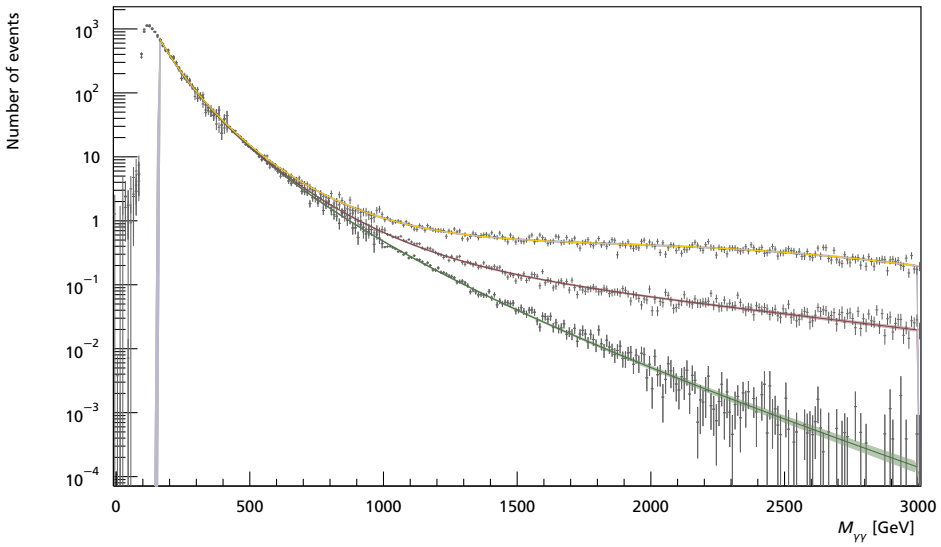

Figure 6.6:
The functions fitted to each of the CalcHEP distributions with different Λ values of 0.75 TeV (yellow), 1.00 TeV (red) and ∞ (the SM, green). The fit is carried out in the range $150 \leq M_{\gamma\gamma} \leq 3000$ TeV. The fit has χ^2 / Ndf = 938.8 / 814.

$$
\begin{aligned}
p_{11} &= 2199 \pm 61 \\
p_{12} &= 740 \pm 86 \\
p_{13} &= -7.6 \pm 0.7 \\
p_{14} &= -0.39 \pm 0.08
\end{aligned}
$$

The error bands in fig. 6.6 represent the 95% confidence intervals on the functions, as calculated from the covariance matrix produced by the fitting procedure. This confidence interval represents the systematic uncertainty that arises from the uncertainty on the fit parameters.

It is now a simple matter to determine the polynomial coefficients, which are plotted in fig. 6.7.

6.3 Maximum likelihood fit

To determine the most likely value of Λ, we will use a maximum likelihood fit to attempt to find the value of Λ that best fits the data.

A full description of the maximum likelihood method is given in [39] or [40]. In brief, the probability of observing a number n_{data} events, given an expected number N_{exp}, is, for a single bin, given by Poisson statistics:

$$p(n_{\text{data}}|N_{\text{exp}}) = \frac{N_{\text{exp}}^{n_{\text{data}}}}{n_{\text{data}}!} e^{-N_{\text{exp}}} \tag{6.5}$$

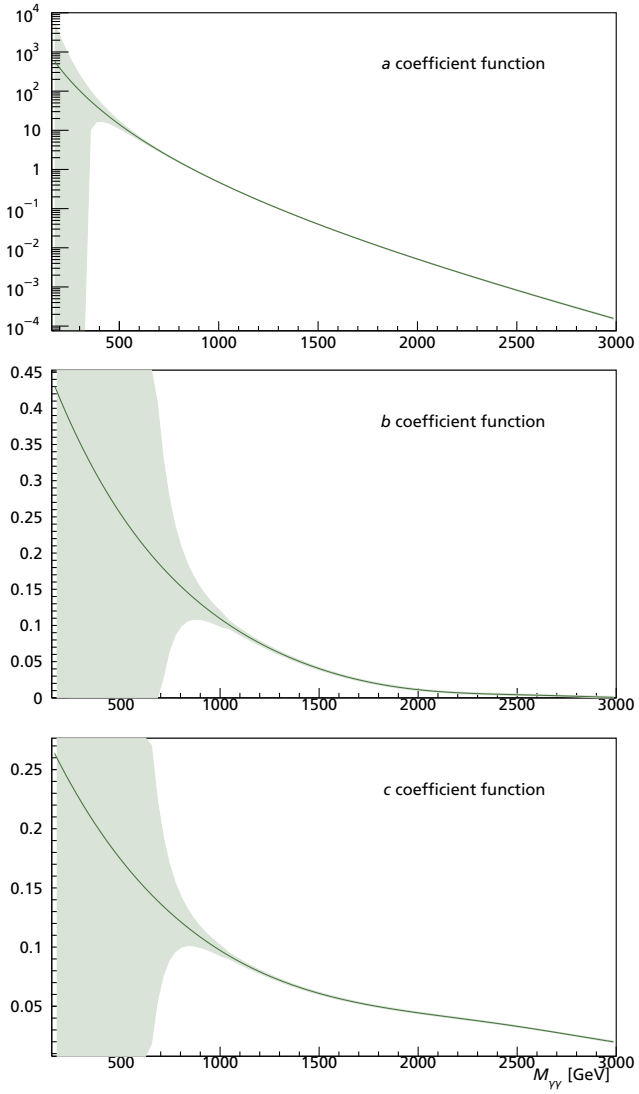

Figure 6.7:
From top to bottom, plots of the coefficients to the constant, linear and quadratic terms used to derive distributions of $M_{\gamma\gamma}$ at any Λ, defined in eq. (2.21), with uncertainties.

In our case, where the experiment has been carried out, n_{data} will be fixed as the value in each bin. Meanwhile, we worked out a method for varying the number of expected events N_{exp} as a function of Λ above. Thus, the most likely value of Λ is the one that maximises equation (6.5). Taking the logarithm of eq. (6.5) yields

$$\ln[p(n_{\text{data}}|N_{\text{exp}})] = -\ln n_{\text{data}}! + n_{\text{data}} \ln N_{\text{exp}} - N_{\text{exp}}, \tag{6.6}$$

where obviously the logarithm of $n_{\text{data}}!$ is a constant for any given bin. Taking the logarithm also allows us to write the likelihood of an ensemble of measured and expected event counts, such as we find in our histograms, as a sum. Finding the value of Λ with the highest likelihood associated is now a simple matter of varying our prediction until we discover a maximum.

As a practical matter, since numerical algorithms for extremum finding are actually minimisers, we will write the negative likelihood,

$$-\ln p,$$

and attempt to find a value of Λ that minimises this number.

We can find a confidence interval around the most likely value by determining what the ratio of likelihoods, or difference of log likelihoods, between the most likely value and the value that corresponds to the desired confidence level,

$$-LLR = \frac{\ln p}{\ln p_{\max}} = n_{\text{data}}(\ln N - \ln N_{\max}) + \ln N_{\max} - \ln N, \tag{6.7}$$

writing $-LLR$ for the negative log likelihood ratio, and dropping the labels on N_{exp} for legibility.

The log ratio of the likelihood of a χ^2 distribution at its mean to its likelihood at the 95th percentile is 3.84 [40]. We adopt this as the best estimate available for the 95% confidence level for twice the negative log likelihood ratio for our distributions as well. The factor two arises from taking the logarithm of χ^2.

As an example, figure 6.8 plots the negative log likelihood ratios associated with searching for the most likely value of Λ given our dataset.

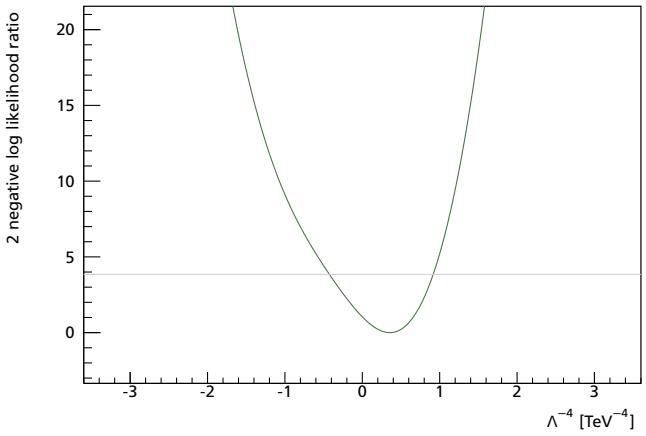

Figure 6.8:
The negative log likelihood ratio times 2, for the likelihood scan over a range of values for Λ^{-4}. This likelihood scan does not include any uncertainties. The minimum negative likelihood corresponds to $\Lambda^{-4} = 0.356$ TeV^{-4}, with a confidence interval of $-0.425 \leq \Lambda^{-4} \leq 0.916$ TeV^{-4}. The horizontal line indicates the log likelihood ratio at the 95% confidence level.

This likelihood fit suggest that the most likely value of Λ is 1.29 TeV, with a lower limit on the 95% confidence interval of 1.02 TeV. That the confidence interval for Λ^{-4} spans across zero indicates that the Standard Model case lies within the confidence interval.

Additional uncertainties can be incorporated into the determination of the log likelihood ratio by introducing nuisance parameters. Say that, in addition to the likelihood associated with the Poisson distribution of observed events n_{data}, the likelihood of a given expected event count N_{exp} also depends on a second distribution $\hat{\mu}$. For a single bin, we modify the number of expected events by a number μ drawn from the $\hat{\mu}$ distribution, and modify the overall likelihood by the likelihood for drawing that μ:

$$p(n_{\text{data}}|N_{\text{exp}}, \mu) = p(n_{\text{data}}|N_{\text{exp}} + \mu)p(\mu) \tag{6.8}$$

Then, to find the likelihood at a step in N_{exp}, we must find the value of μ that minimises the total negative log likelihood. We assign separate $\hat{\mu}$ distributions for each bin in a histogram. Thus, for a histogram with bins i, the negative log likelihood is given by

$$-LL = \sum_i \ln n_i! - n_i \ln(N_i + \mu_i) + (N_i + \mu_i) - \ln p_i(\mu_i), \tag{6.9}$$

where, for each bin i, μ_i is selected to minimise this expression. This is known as the profile log likelihood. The negative log likelihood ratio will then be between the value of this expression at a given N_{exp} and the value with the N_{exp} that minimises this expression.

As is common with error distributions, $\hat{\mu}$ is usually assumed to be a Gaussian distribution, an assumption that we will also make in the following.

6.3.1 Systematic uncertainties

In the course of developing the MC sets used, we identified a number of systematic uncertainties that should be included at this point.

We will, in the absence of better information, assume that all systematic uncertainties are uncorrelated, and, unless otherwise noted, that individual uncertainties are completely correlated across all bins. These uncertainties will then be included as nuisance parameters in the log likelihood fit, by constructing a simple Gaussian distribution of appropriate width about n_{data} for each systematic in each bin, and then combining them. In practice, this means adding together their standard deviations in quadrature.

To summarise, the systematic uncertainties were:

- Choice of PDF: Table 3.1 summarises the uncertainties determined due to our choice of PDF. Since we have identified separate errors for each Λ sample, we will apply this effect to the appropriate $M_{\gamma\gamma}$ function before determining the errors on the coefficient functions. Thus, this effect of this systematic uncertainty is included in the error on the coefficient functions illustrated in fig. 6.7.

- Reweighting: By taking the root–square–sum of the error on the weight assigned to each event in a bin in $M_{\gamma\gamma}$, we were able to ascertain the systematic uncertainty due to the reweighting procedures above bin–by–bin for each Λ sample.

- Confidence interval on $M_{\gamma\gamma}$ shape functions: Potentially, these could be evaluated separately for each value of Λ.

- Choice of event generator: We have attempted to minimise the effect of generator choice by actively tuning CalcHEP to produce distributions of events similar to pythia. A systematic error of 9.18% on the overall event count is included to account for the deviation of the MadGraph sample.

In addition, we include systematic uncertainties due to the following detector effects:

- Photon identification: 1.5%
- Uncertainty on luminosity: 2.8%

The systematic uncertainties which were determined for each Λ distribution individually, namely the confidence interval on the fitted functions, the PDF uncertainty and the uncertainty due to the reweighting procedure, were applied as systematic errors to the functions fitted to the distributions in figure 6.6, and converted to systematic errors on the coefficient functions, plotted in fig. 6.7, through standard error propagation. Potentially, the resulting errors on the $M_{\gamma\gamma}$ distributions constructed from these coefficient functions could be determined for each Λ individually, however, this proves too cumbersome to implement. In stead, we take as a conservative estimate the uncertainty associated with a function constructed for $\Lambda^{-4} = 3.0$ TeV^{-4}, which is the upper limit on values of Λ^{-4} searched by the minimiser. When determining errors associated with a distribution of invariant mass constructed from the parametrisation at a given value of Λ, the uncertainty associated with the b and c coefficient functions will enter into the uncertainty on the constructed distribution proportionally to Λ^{-4} and $(\Lambda^{-4})^2$, respectively. Thus, we expect the distribution constructed for large values of Λ to have larger uncertainties associated with them, and choose the errors associated with the highest value of Λ^{-4} searched as the conservative estimate for this error. This uncertainty is evaluated for each bin in $M_{\gamma\gamma}$. The uncertainties thus arrived at are combined with the overall uncertainties from the choice of event generator and detector effects, and applied as nuisance parameters in the log likelihood fit. Since these uncertainties include effects that are not assumed to be correlated between bins, the uncertainties on each bin are treated as separate nuisance parameters. The histograms being fitted in the next section contain 90 bins, meaning that the fit takes into account 90 nuisance parameters.

For the background sample, by far the dominant source of uncertainty is that arising from limited statistics in the γjet sample. As such, we will use it as a first approximation of the total uncertainty.

6.4 Setting a limit

Figure 6.9 shows the negative profile log likelihood values found scanning over values for Λ^{-4} corresponding to $\Lambda = \pm 760$ GeV.

As figure 6.9 states, this result excludes the Standard Model. To achieve this result, we have neglected the considerable statistical uncertainty contributed by the γjet sample, as is clear from table 5.1. This uncertainty can be accounted for by incorporating it as a second set of nuisance parameters associated with the background sample. This will require significantly more CPU time to compute than the result presented above.

Figure 6.10 shows the $M_{\gamma\gamma}$ distribution associated with the most likely value of Λ, along with those associated with the limits on the confidence interval overlaid on the data distribution.

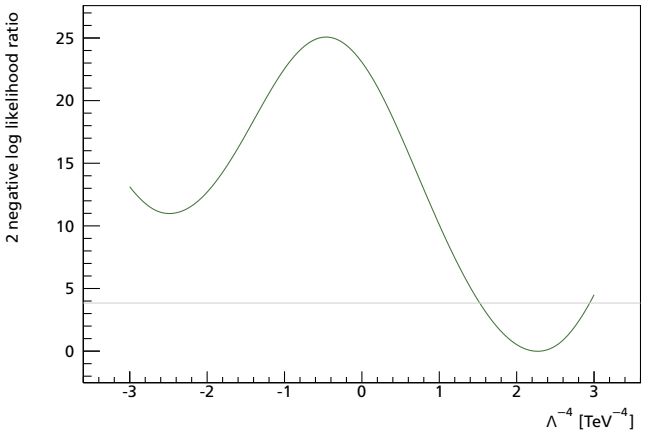

Figure 6.9:
The negative 2 log likelihood ratio for the profile likelihood scan over a range of values for Λ^{-4}. This likelihood scan does not include uncertainties on the background. The minimum negative likelihood corresponds to $\Lambda = 814$ GeV, with a confidence interval of $763 \leq \Lambda \leq 900$ GeV. The horizontal line indicates the log likelihood ratio at the 95% confidence level.

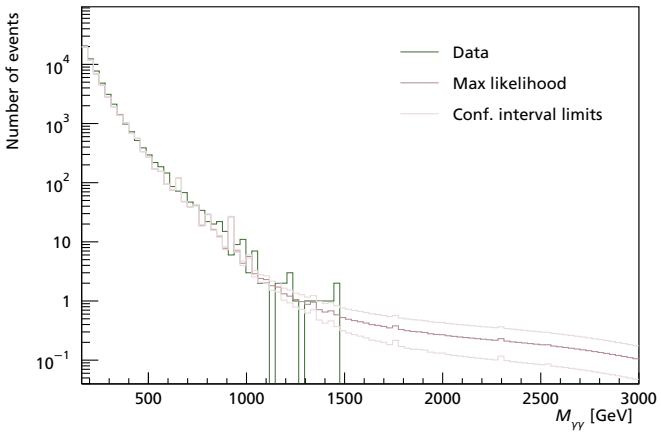

Figure 6.10:
The data distribution of $M_{\gamma\gamma}$ overlaid with the constructed distributions at the most likely value of Λ and at the limits of the confidence level.

6.5 Addendum: additional results

As was noted above, the profile log likelihood fit which takes into account also the uncertainties on the background distribution was too computationally intensive to be completed in time for the initial publication of this thesis. Between then and the thesis defence, this result did become available, however, and is presented here.

Due to its magnitude, the systematic uncertainty on the background sample will be given solely by the uncertainty that arises from limited statistics in the ATLAS γjet sample. The uncertainty on this sample was illustrated in figure 5.6. Figure 6.11 shows the effect on the distributions shown in figure 6.4 of adding in the γjet MC set. These distributions are compatible within their errors.

Due to limitations of the minimiser used, this profile log likelihood fit has required a rebinning of the distributions used down to 50 bins. The 2 negative log likelihood scan is shown in figure 6.12, while the resulting most likely distribution and confidence interval are overlaid on the data distribution in figure 6.13.

Unlike the previous result, this result, which includes all systematic uncertainties considered in the thesis, does not exclude the Standard Model. We find a lower limit

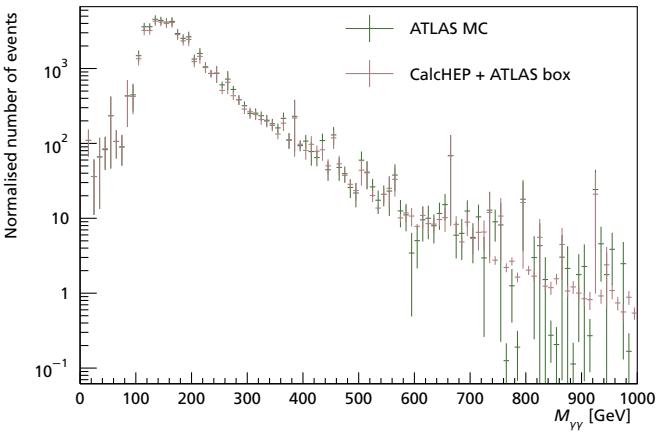

Figure 6.11:
Comparing the ATLAS distribution with the one produced by CalcHEP, combined with a distribution for the box diagram contribution. The ATLAS γjet MC set has here been added to both distributions.

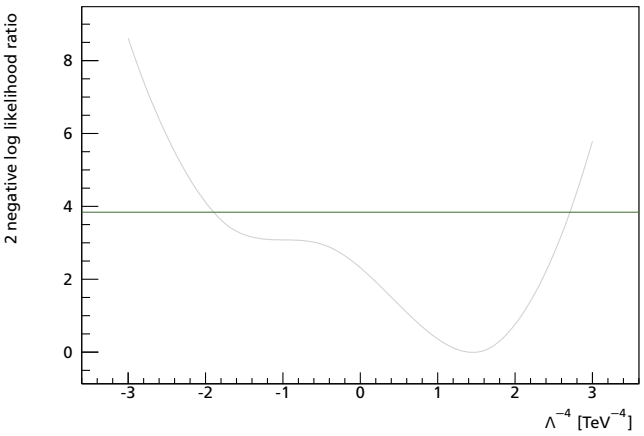

Figure 6.12:
The negative 2 log likelihood ratio for the profile likelihood scan over a range of values for Λ^{-4}. This likelihood scan includes uncertainties on the background, but uses a coarser binning than the previous result. The minimum negative likelihood occurs at $\Lambda^{-4} = 1.49$ [GeV^{-4}], the lower bound of the confidence interval is at $\Lambda^{-4} = -1.89$, and the upper limit is at $\Lambda^{-4} = 2.71$ [GeV^{-4}]. The horizontal line indicates the log likelihood ratio at the 95% confidence level.

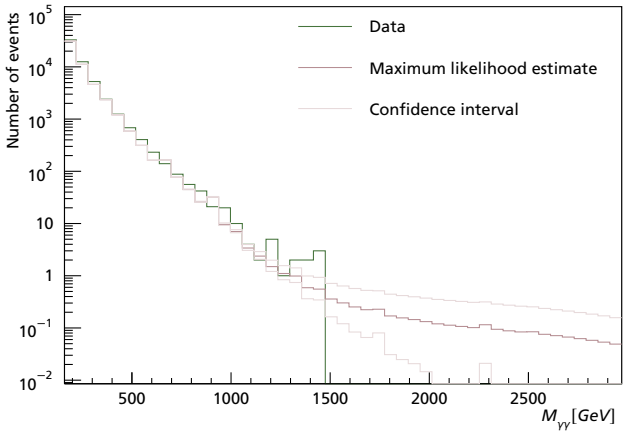

Figure 6.13:
The data distribution of $M_{\gamma\gamma}$ overlaid with the constructed distributions at the most likely value of Λ and at the limits of the confidence level, in the fit which includes the uncertainty on the background distribution.

on Λ, at the 95% confidence level, of 779 GeV.

7 Conclusion

In this thesis, we attempted to estimate the effect of a $qq \to \gamma\gamma$ contact interaction, with associated energy scale Λ, upon the distribution of $M_{\gamma\gamma}$ in diphoton events produced in proton–proton collisions at the LHC.

The new interaction was introduced in a modified Standard Model through the effective Lagrangian approach.

This is a highly non–trivial endeavour, as there are no suitable ATLAS Monte Carlo sets on which to base this attempt. We found that even the Monte Carlo set created to simulate the Standard Model $qq \to \gamma\gamma$ process did not satisfactorily cover the sensitive region at high invariant masses. Thus, we were required to go through every step needed to create a suitable MC data set. This process involved long processing times, using large and cumbersome software packages. In the end, there is room for improvement in the outcome of this process.

We exploited the quadratic form of the expression for the strength of the new interaction to derive a shape for the distribution of events at arbitrary Λ from distributions created at two discrete values of Λ and the Standard Model distribution. This involved describing the shape of the distribution by performing a simultaneous fit over all three distributions.

A data driven background estimation technique was applied to data taken from the ATLAS detector at the LHC. The resulting estimated background distribution was combined with appropriate distributions from Monte Carlo, and its shape was extrapolated into the sensitive invariant mass region above 1 000 GeV.

A most likely value of Λ, with accompanying confidence interval was found by comparing the data distribution of invariant mass, $M_{\gamma\gamma}$, with the Monte Carlo distribution, combined with appropriate backgrounds, using a maximum profile likelihood procedure, which took systematic uncertainties into account. The invariant mass was chosen as the discriminating variable among several other variables, for its discriminating power and robustness.

The profile likelihood fit give as a result a 95% confidence interval for Λ between 763 and 900 GeV. This result is influenced by the poor statistics and high uncertainty in the signal region of the ATLAS γjet Monte Carlo sample. The result could be improved if a sample with better statistics were available. We have also pointed a direction for better accounting for the uncertainty associated with this sample in the context of a likelihood profile fit.

The analysis already included methods that produced errors for bins individually,

rather than assuming correlation across all bins. This process is easily extended to accept per–bin or per–event uncertainties for detector effects or Monte Carlo uncertainties. It can also be extended to account for correlated errors.

Lastly, an analysis similar to this one on the data from 13 TeV collisions being taken at the LHC this year (2015) would of course have substantially better sensitivity due to the strong enhancement with energy.

7.1 Addendum

An additional estimate for the confidence limits on Λ became available before the thesis defence. A profile likelihood fit which included uncertainties on the background distribution finds a confidence interval for Λ which agrees with the Standard Model, and sets a lower limit on Λ of 779 GeV.

References

[1] Wikipedia. *Standard Model*. URL: http://en.wikipedia.org/w/index.php?title=Standard_Model&oldid=592640485.

[2] Herbert Goldstein, Charles P. Poole, and John L. Safko. *Classical Mechanics*. 3rd. Addison-Wesley, June 25, 2001. ISBN: 0201657023. URL: http://www.worldcat.org/isbn/0201657023.

[3] Mark Srednicki. *Quantum Field Theory*. Fourth edition. Cambridge University Press, 2010.

[4] Jorge C. Romao and Joao P. Silva. „A resource for signs and Feynman diagrams of the Standard Model“. In: *Int. J. Mod. Phys.* A27 (2012), p. 1230025. DOI: 10.1142/S0217751X12300256. arXiv: 1209.6213 [hep-ph].

[5] A. Semenov. „LanHEP: A Package for the automatic generation of Feynman rules in field theory. Version 3.0“. In: *Comput.Phys.Commun.* 180 (2009), pp. 431–454. DOI: 10.1016/j.cpc.2008.10.012. arXiv: 0805.0555 [hep-ph]. URL: http://theory.sinp.msu.ru/~semenov/lanhep.html.

[6] Adam Alloul et al. „FeynRules 2.0 - A complete toolbox for tree-level phenomenology“. In: (2013). arXiv: 1310.1921 [hep-ph]. URL: http://feynrules.irmp.ucl.ac.be/.

[7] Thomas G. Rizzo. „Diphoton production at hadron colliders and new contact interactions“. In: *Phys. Rev. D* 51 (3 Feb. 1995), pp. 1064–1067. DOI: 10.1103/PhysRevD.51.1064. URL: http://link.aps.org/doi/10.1103/PhysRevD.51.1064.

[8] B. R. Martin and G. Shaw. *Particle Physics*. Third. Wiley, 2008.

[9] Ernest Rutherford. „The Scattering of α and β Particles by Matter and the Structure of the Atom“. In: *Philosophical Magazine*. 6th ser. 21 (May 1911). URL: http://www.lawebdefisica.com/arts/structureatom.pdf.

[10] Durham HEPData Project. *PDF Plotter*. URL: http://hepdata.cedar.ac.uk/pdf/pdf3.html.

[11] Dan Green. *High p_T Physics at Hadron Colliders*. Cambridge University Press, 2005.

[12] Alexander Belyaev, Neil D. Christensen, and Alexander Pukhov. „CalcHEP 3.4 for collider physics within and beyond the Standard Model“. In: *Comput.Phys.Commun.* 184 (2013), pp. 1729–1769. arXiv: 1207.6082 [hep-ph]. URL: http://theory.sinp.msu.ru/~pukhov/calchep.html.

[13] Johan Alwall et al. „MadGraph 5 : Going Beyond“. In: *JHEP* 1106 (2011), p. 128. DOI: 10.1007/JHEP06(2011)128. arXiv: 1106.0522 [hep-ph]. URL: http://madgraph.hep.uiuc.edu/.

[14] Torbjörn Sjöstrand. *Pythia Website*. URL: http://home.thep.lu.se/~torbjorn/Pythia.html.

[15] Andy Buckley et al. „Rivet user manual“. In: *Comput.Phys.Commun.* 184 (2013), pp. 2803–2819. DOI: 10.1016/j.cpc.2013.05.021. arXiv: 1003.0694 [hep-ph].

[16] John C. Collins and Davison E. Soper. „Angular distribution of dileptons in high-energy hadron collisions“. In: *PHYSICAL REVIEW D* 16.7 (1977).

[17] Dieter Zeppenfeld. *PiTP Lectures*. 2005. URL: http://www.gk-eichtheorien.physik.uni-mainz.de/Dateien/Zeppenfeld-3.pdf.

[18] Torbjörn Sjöstrand, Stephen Mrenna, and Peter Skands. „PYTHIA 6.4 physics and manual“. In: *Journal of High Energy Physics* 2006.05 (2006), p. 026. URL: http://stacks.iop.org/1126-6708/2006/i=05/a=026.

[19] CERN. *The LHC Guide*. CERN website. URL: http://cds.cern.ch/record/1165534/files/CERN-Brochure-2009-003-Eng.pdf.

[20] CERN. *Experiments | CERN*. CERN website. URL: http://home.web.cern.ch/about/experiments.

[21] Peter Hansen. „Particle detectors and accelerators“. Lecture notes, University of Copenhagen. 2015.

[22] ATLAS Collaboration. ATLAS *website*. URL: atlas.ch.

[23] ATLAS Collaboration. „The ATLAS Experiment at the CERN Large Hadron Collider“. In: *Journal of Instrumentation* 3.08 (2008), S08003. URL: http://stacks.iop.org/1748-0221/3/i=08/a=S08003.

[24] Richard Fernow. In: *Introduction to experimental particle physics*. Cambridge University Press, 1986. Chap. 11.

[25] Ulrik Egede. „The search for a standard model Higgs at the LHC and electron identification using transition radiation in the ATLAS tracker“. MA thesis. Lund Univerity, 1997. URL: http://www.hep.lu.se/atlas/thesis/egede/thesis.html.

[26] WolframAlpha. URL: http://www.wolframalpha.com/input/?i=1.6MiB/50ns.

[27] ATLAS Collaboration. *Luminosity Public Results*. ATLAS Twiki. URL: https://twiki.cern.ch/twiki/bin/view/AtlasPublic/LuminosityPublicResults.

[28] ATLAS Collaboration. „ATLAS e/gamma twiki page“. URL: https://twiki.cern.ch/twiki/bin/view/AtlasProtected/ElectronGamma.

[29] ATLAS Collaboration. *Expected photon performance in the* ATLAS *experiment*. ATL-PHYS-PUB-2011-007. 2011. URL: http://cdsweb.cern.ch/record/1345329.

[30] W Lampl et al. „Calorimeter Clustering Algorithms: Description and Performance“. In: ATL-LARG-PUB-2008-002. ATL-COM-LARG-2008-003. Geneva, Apr. 2008. Chap. 2.1. URL: https://cds.cern.ch/record/1099735.

[31] L Carminati et al. *Reconstruction and Identification Efficiency of Inclusive Isolated Photons*. Tech. rep. ATL-COM-PHYS-2010-803. Geneva: CERN, Oct. 2010.

[32] William Buttinger. *Using Event Weights to account for differences in Instantaneous Luminosity and Trigger Prescale in Monte Carlo and Data*. Tech. rep. ATL-COM-SOFT-2015-119. Geneva: CERN, May 2015. URL: https://cds.cern.ch/record/2014726.

[33] S. Agostinelli et al. „Geant4—a simulation toolkit“. In: *Nuclear Instruments and Methods in Physics Research Section A: Accelerators, Spectrometers, Detectors and Associated Equipment* 506.3 (2003), pp. 250–303. ISSN: 0168-9002. DOI: http://dx.doi.org/10.1016/S0168-9002(03)01368-8. URL: http://www.sciencedirect.com/science/article/pii/S0168900203013688.

[34] ATLAS Collaboration. „Electron and photon energy calibration with the ATLAS detector using LHC Run 1 data“. In: *Eur. Phys. J.* C74.10 (2014), p. 3071. DOI: 10.1140/epjc/s10052-014-3071-4. arXiv: 1407.5063 [hep-ex].

[35] M. Aurousseau et al. „First evidence of direct diphoton production in pp collisions at $\sqrt{s} = 7$ TeV in ATLAS“. In: ATLAS *note* (2010).

[36] M. Cepeda et al. „Data driven methods for QCD background estimation in electroweak muon analysis; the ABCD and the template methods“. In: *CMS Analysis Note* CMS-AN-2008-113 (2008).

[37] T. Aaltonen et al. „Search for new particles decaying into dijets in proton-antiproton collisions at s**(1/2) = 1.96-TeV“. In: *Phys. Rev.* D79 (2009), p. 112002. DOI: 10.1103/PhysRevD.79.112002. arXiv: 0812.4036 [hep-ex].

[38] CERN. *ROOT website*. URL: root.cern.ch.

[39] R. J. Barlow. *Statistics: A guide to the use of statistical methods in the physical sciences*. Wiley, 1989. ISBN: 0471922951.

[40] A B Balantekin and Particle Data Group. „Review of Particle Physics“. In: *Journal of Physics G: Nuclear and Particle Physics* 33 (2006).

A ATLAS Monte Carlo data sets

This appendix contains the full identifiers of the ATLAS Monte Carlo data sets used in this thesis.

A.1 Gamma–gamma set

_8TeV.129180.Pythia8_AU2CTEQ6L1_gammagamma_2DP20.merge.
NTUP_PHOTON.e1199_s1482_s1473_r3542_r3549_p1344

A.2 Box gamma–gamma set

_8TeV.146800.Pythia8_AU2CTEQ6L1_GamGamBox_pT35pT20.merge.
NTUP_PHOTON.e1222_s1469_s1470_r3542_r3549_p1344

A.3 Gamma–jet sets

_8TeV.129170.Pythia8_AU2CTEQ6L1_gammajet_DP17.merge.
NTUP_PHOTON.e1146_s1468_s1470_r3542_r3549_p1344

_8TeV.129171.Pythia8_AU2CTEQ6L1_gammajet_DP35.merge.
NTUP_PHOTON.e1146_s1468_s1470_r3542_r3549_p1344

_8TeV.129172.Pythia8_AU2CTEQ6L1_gammajet_DP70.merge.
NTUP_PHOTON.e1146_s1468_s1470_r3542_r3549_p1344

_8TeV.129173.Pythia8_AU2CTEQ6L1_gammajet_DP140.merge.
NTUP_PHOTON.e1146_s1468_s1470_r3542_r3549_p1344

_8TeV.129174.Pythia8_AU2CTEQ6L1_gammajet_DP280.merge.
NTUP_PHOTON.e1146_s1468_s1470_r3542_r3549_p1344

_8TeV.129175.Pythia8_AU2CTEQ6L1_gammajet_DP500.merge.
NTUP_PHOTON.e1146_s1468_s1470_r3542_r3549_p1344

A.4 Z to ee set

_8TeV.147770.Sherpa_CT10_Zee.merge.
NTUP_PHOTON.e1434_s1499_s1504_r3658_r3549_p1344.

A.5 Sets examined for potential backgrounds

_8TeV.107680.AlpgenJimmy_AUET2CTEQ6L1_WenuNp0.merge.
NTUP_PHOTON.e1218_s1469_s1470_r3542_r3549_p1344.
_8TeV.107684.AlpgenJimmy_AUET2CTEQ6L1_WenuNp4.merge.
NTUP_PHOTON.e1218_s1469_s1470_r3542_r3549_p1344.
_8TeV.113714.Sherpa_CT10_SinglePhotonPt35.merge.
NTUP_PHOTON.e1249_s1469_s1470_r3542_r3549_p1344.31.05.130531160824
_8TeV.113715.Sherpa_CT10_SinglePhotonPt70.merge.
NTUP_PHOTON.e1249_s1469_s1470_r3542_r3549_p1344.31.05.130531160856
_8TeV.113716.Sherpa_CT10_SinglePhotonPt140.merge.
NTUP_PHOTON.e1249_s1469_s1470_r3542_r3549_p1344.31.05.130531160931
_8TeV.113717.Sherpa_CT10_SinglePhotonPt280.merge.
NTUP_PHOTON.e1249_s1469_s1470_r3542_r3549_p1344.31.05.130531161030
_8TeV.126371.Sherpa_CT10_SinglePhotonPt500.merge.
NTUP_PHOTON.e1249_s1469_s1470_r3542_r3549_p1344.31.05.130531161224
_8TeV.126372.Sherpa_CT10_SinglePhotonPt15.merge.
NTUP_PHOTON.e1249_s1469_s1470_r3542_r3549_p1344.31.05.130531161146
_8TeV.126955.Sherpa_CT10_SinglePhotonPt800.merge.
NTUP_PHOTON.e1249_s1469_s1470_r3542_r3549_p1344.31.05.130531161311
_8TeV.126956.Sherpa_CT10_SinglePhotonPt1000.merge.
NTUP_PHOTON.e1249_s1469_s1470_r3752_r3549_p1344.31.05.130531161341
_8TeV.128495.AlpgenPythia_P2011CCTEQ6L1_GamGamMass50GeVNp0.merge.
NTUP_PHOTON.e1222_s1469_s1470_r3542_r3549_p1344.
_8TeV.128496.AlpgenPythia_P2011CCTEQ6L1_GamGamMass50GeVNp1.merge.
NTUP_PHOTON.e1222_s1469_s1470_r3542_r3549_p1344.
_8TeV.128497.AlpgenPythia_P2011CCTEQ6L1_GamGamMass50GeVNp2.merge.
NTUP_PHOTON.e1222_s1469_s1470_r3542_r3549_p1344.
_8TeV.128498.AlpgenPythia_P2011CCTEQ6L1_GamGamMass50GeVNp3.merge.
NTUP_PHOTON.e1222_s1469_s1470_r3542_r3549_p1344.
_8TeV.146431.AlpgenJimmy_AUET2CTEQ6L1_WgammaNp1.merge.
NTUP_PHOTON.e1260_s1469_s1470_r3542_r3549_p1344.
_8TeV.146433.AlpgenJimmy_AUET2CTEQ6L1_WgammaNp3.merge.
NTUP_PHOTON.e1293_s1469_s1470_r3542_r3549_p1344.
_8TeV.146434.AlpgenJimmy_AUET2CTEQ6L1_WgammaNp4.merge.
NTUP_PHOTON.e1293_s1469_s1470_r3542_r3549_p1344.
_8TeV.146435.AlpgenJimmy_AUET2CTEQ6L1_WgammaNp5.merge.
NTUP_PHOTON.e1293_s1469_s1470_r3542_r3549_p1344.

_8TeV.146824.Sherpa_CT10_2DP20_3j_Myy80GeV.merge.
NTUP_PHOTON.e1434_s1499_s1504_r3658_r3549_p1344.
_8TeV.146825.Sherpa_CT10_SinglePhotonPt15_2JetEt35Et20.merge.
NTUP_PHOTON.e1310_s1469_s1470_r3542_r3549_p1344.31.05.130531161104
_8TeV.147364.Sherpa_CT10_Zeegammagamma.merge.
NTUP_PHOTON.e1972_s1581_s1586_r3658_r3549_p1344.
_8TeV.147771.Sherpa_CT10_Zmumu.merge.
NTUP_PHOTON.e1434_s1499_s1504_r3658_r3549_p1344.
_8TeV.147800.PowhegPythia8_AU2CT10_Wplusenu.merge.
NTUP_PHOTON.e1169_s1482_s1473_r3542_r3549_p1344.31.05.130531160433
_8TeV.147803.PowhegPythia8_AU2CT10_Wminenu.merge.
NTUP_PHOTON.e1169_s1482_s1473_r3542_r3549_p1344.31.05.130531160506
_8TeV.147806.PowhegPythia8_AU2CT10_Zee.merge.
NTUP_PHOTON.e1169_s1482_s1473_r3542_r3549_p1344.31.05.130531160538
_8TeV.147807.PowhegPythia8_AU2CT10_Zmumu.merge.
NTUP_PHOTON.e1169_s1469_s1470_r3542_r3549_p1344.
_8TeV.147808.PowhegPythia8_AU2CT10_Ztautau.merge.
NTUP_PHOTON.e1169_s1469_s1470_r3542_r3549_p1344.
_8TeV.158728.Sherpa_CT10_ZeegammaPt70.merge.
NTUP_PHOTON.e1518_s1499_s1504_r3658_r3549_p1344.
_8TeV.167476.Sherpa_CT10_Zeegammagamma.merge.
NTUP_PHOTON.e1531_s1499_s1504_r3658_r3549_p1344.
_8TeV.167477.Sherpa_CT10_Zmumugammagamma.merge.
NTUP_PHOTON.e1531_s1499_s1504_r3658_r3549_p1344.
_8TeV.167478.Sherpa_CT10_Ztautaugammagamma.merge.
NTUP_PHOTON.e1573_s1499_s1504_r3658_r3549_p1344.
_8TeV.167479.Sherpa_CT10_Znunugammagamma.merge.
NTUP_PHOTON.e1531_s1499_s1504_r3658_r3549_p1344.
_8TeV.169707.MadgraphPythia_AUET2B_CTEQ6L1_Wgam0jj_fullme.merge.
NTUP_PHOTON.e1788_s1581_s1586_r3658_r3549_p1344.
_8TeV.181080.Sherpa_CT10_ZeegammaPt25.merge.
NTUP_PHOTON.e1978_s1581_s1586_r3658_r3549_p1344.

This is version 2 of the thesis, which contains minor corrections and additional results which became available before the thesis defence on 30 october 2015.